2008-01-1602
SAND2008-2316C

In-cylinder CO and UHC Imaging in a Light-Duty Diesel Engine during PPCI Low-Temperature Combustion

Duksang Kim, Isaac Ekoto, William F. Colban, Paul C. Miles
Sandia National Laboratories

ABSTRACT

Two-dimensional planar imaging and one-dimensional, spectrally-resolved line-imaging of laser-induced fluorescence from CO and UHC are performed to help identify the sources of these emissions in a light-duty diesel engine operating in a partially-premixed compression ignition combustion regime. Cycle-averaged measurements are made in the clearance volume above the piston crown at a 3 bar IMEP, 1500 rpm baseline operating condition. Sweeps of injection timing, load, and O_2 concentration are performed to examine the impact of these parameters on the in-cylinder spatial distributions of CO and UHC.

At the baseline operating condition, the main contributions to UHC from the clearance volume stem from regions near the cylinder centerline and near the cylinder wall, where UHC likely emanates from the top ring-land crevice. Broadly distributed CO within the squish volume dominates over CO observed near the cylinder centerline. Advanced or retarded injection forms rich or over-lean mixtures, respectively, in the squish volume—resulting in increased UHC from this region. Advanced injection produces more CO in the squish volume; retarded injection initially produces less. Later in the cycle, higher CO levels are observed with retarded injection than in the baseline case. Increased load richens the mixture in the squish volume region, with little impact on UHC but a reduction in CO. Decreased load results in increased UHC and CO in the squish volume and, eventually, at all radial locations. With decreased O_2 concentration, UHC and CO are generally increased throughout the cylinder; combustion within the squish volume is particularly impacted by dilution.

Engine-out emission levels deduced from fluorescence measurements made during the exhaust process are also shown to correlate well with conventional exhaust gas emissions measurements.

INTRODUCTION

In the past decade, significant effort has been devoted to achieving simultaneous reduction of particulate matter (PM) and nitric oxide (NO_x) emissions from high-speed direct-injection (HSDI) diesel engines. Diesel particulate filters and selective catalytic reduction of NO_x are now available for after-treatment of HSDI engine exhaust. Nevertheless, to minimize the cost and complexity of exhaust after-treatment systems—as well as potential fuel economy penalties—considerable research effort has also focused on the in-cylinder control of emissions through the application of low-temperature combustion techniques.

The “smokeless” diesel [1] or partially-premixed compression ignition (PPCI) [2] combustion system is one example of the in-cylinder control of PM and NO_x formation by maintaining low peak combustion temperatures. In PPCI combustion, high amounts of EGR (often 60% or more of the total intake mass) result in a low charge O_2 concentration. This heavy charge dilution is the major factor responsible for keeping peak combustion temperatures low. Moreover, due to the low O_2 concentration, the ignition delay of the injected fuel is lengthened, promoting the formation of a more homogeneous mixture. A long ignition delay may, however, result in the formation of overly fuel lean regions, which can lead to excessive CO and UHC emissions. In addition, it can lead to high levels of combustion noise, although this is moderated by reduced peak heat release rate due to the low temperatures and dilute mixtures.

Overly lean mixtures are not the only potential source of CO and UHC emissions in PPCI combustion systems. The highly-dilute charge also requires that a significantly larger charge mass be mixed with the fuel to achieve complete combustion. If mixing processes are not sufficiently rapid, or an inappropriate bulk fuel distribution is formed, significant emissions may also result from overly fuel rich regions with $\phi > 1$. Previous studies of the CO emissions from automotive diesel engines operating in a PPCI combustion regime have shown that CO emissions can be strongly influenced by mixing processes, particularly processes that influence the bulk fuel distribution in the cylinder [3,4,5]. In addition, with a sufficiently dilute intake charge, CO emissions are negatively correlated with ignition delay—that is, increased ignition delay reduces CO emissions [3]. These observations, coupled with the results of

multi-dimensional simulations [4,5], suggest that a significant fraction of the CO and UHC emissions may stem from overly rich regions caused by insufficient mixing.

This paper employs both homogeneous reactor modeling of n-C_7H_{16} oxidation and in-cylinder measurements of cycle-averaged spatial distributions of CO and UHC to help clarify the sources of CO and UHC emissions in light-duty PPCI combustion systems. The measurements are obtained during the expansion and exhaust stroke via imaging of laser induced fluorescence (LIF). Variations in injection timing, load, and O_2 concentration about a typical PPCI operating condition are explored to determine how these parameters influence the CO and UHC distributions. The in-cylinder data are also compared with conventionally measured exhaust gas emissions and with cycle-resolved exhaust gas UHC measurements.

HOMOGENEOUS REACTOR MODELING

Figures 1 and 2 show the CO and UHC yield predicted by homogeneous reactor simulations conducted at constant temperature and pressure, for various temperatures and initial mixture equivalence ratios. Regions of soot and NO_x formation, as computed by Kitamura et al. [6] under the same conditions, are also shown for reference. The constant temperature and pressure conditions employed for these calculations are a severe approximation to a heterogeneous engine environment characterized by changing temperature, pressure, and continuous mixing. Nevertheless, the results correspond remarkably well with those obtained from multi-dimensional simulations [8,9] or homogeneous simulations [10] with changing pressure and temperature[†].

The classic sources of CO emissions [11] for conventional diesel combustion are clearly apparent in Fig. 1: overly lean regions that burn slowly and overly rich regions with insufficient O_2 to complete combustion. Lean regions resulting in a high CO yield are observed for temperatures between approximately 800 – 1400 K, while there is significant CO present for rich mixtures ($\phi \gtrsim 1$) at all temperatures high enough to achieve substantial fuel oxidation. Similar behavior is seen in the UHC results shown in Fig. 2—UHC emissions can stem from both overly lean and overly rich regions. Overly lean regions are traditionally thought to be caused by over-mixing during the ignition delay period [12]. Recently, Musculus and co-workers [13] have shown that under conditions characterized by a long ignition delay, a significant fraction of this lean mixture may be formed late in the injection event, when the decreasing, transient jet velocity can cause formation of very lean

[†] The constant temperature and pressure simulations are most problematic at low temperatures and equivalence ratios, where the influence of the negative temperature coefficient (NTC) region near 1000 K is more pronounced than would be found in a more realistic environment where the heat release due to combustion raises the gas temperature.

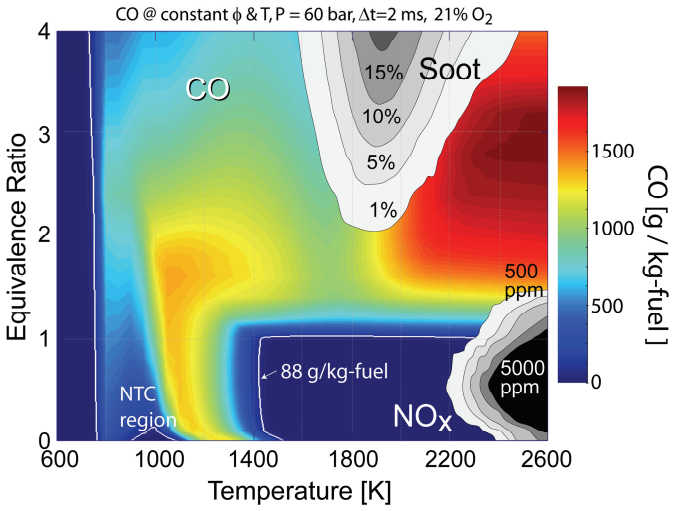

Figure 1 CO yield at 2.0 ms obtained from a homogeneous reactor simulation of an n-heptane-air mixture, using the LLNL detailed n-heptane mechanism [7]. The 88 g/kg-fuel isopleth corresponds to 2% of the fuel energy in CO

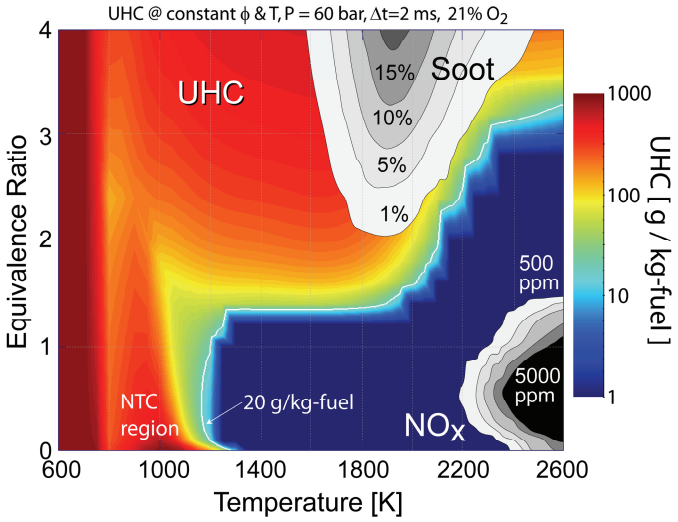

Figure 2 UHC yield for the same conditions as Fig. 1

regions near the injector. UHC emissions from under-mixed, overly rich regions (or regions suffering from delayed mixing) have previously been associated with fuel emanating from the injector holes and sac volume after the injection event [12].

Information about local temperature or mixture stoichiometry can be deduced from the relative behavior of measurements of CO and UHC. Comparing Figs. 1 and 2, two regions of high UHC yield can be identified where CO yield is predicted to be low. The first region is characterized by cold fluid ($T \lesssim 800$ K) over the full range of equivalence ratios. This region corresponds to engine crevices, wall quench layers, and liquid films. For well-optimized, heavy-duty diesel engines, UHC stemming from these sources is considered minor. However, in light-duty engines these sources are thought to be considerably more important [14,15,16]. The second, smaller region is found where NTC

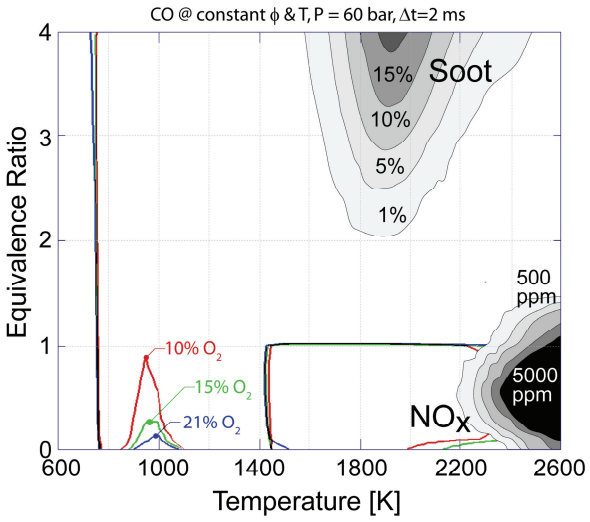

Figure 3 Isopleths of 88 g/kg-fuel CO yield obtained in constant temperature and pressure homogeneous reactor simulations for various dilution levels

behavior slows the low temperature oxidation of UHC as temperature increases, leading to higher UHC yield and inhibiting the production of CO.

For leaner mixtures, as temperature increases above approximately 1000 K, UHC decreases and CO increases rapidly. Consequently, the local maxima in UHC and CO yield are not coincident, but adjacent. Between these maxima, gradients of CO and UHC with temperature are of opposite sign. Likewise, in the colder wall regions, gradients of CO and UHC also differ in sign. The experimental observation of counter-aligned gradients in CO and UHC is thus likely to indicate cooler fluid ($T \lesssim 1100$ K), and—away from the walls—this cooler fluid is most probably associated with lean mixtures. At higher temperatures, between approximately 1200 and 1400 K, UHC oxidation is nearly complete but the CO yield is still significant for these leaner mixtures. High CO yield coupled with low UHC is also found in moderately rich mixtures ($1.0 \lesssim \phi \lesssim 1.3$). In the first case, high CO yield is caused by the slow kinetics of CO oxidation compared to the UHC oxidation. In the latter case, insufficient O_2 is available to complete oxidation, and chemical equilibrium favors species such as CO and H_2 over UHC as incomplete oxidation products.

The influence of dilution with the products of complete combustion on the CO and UHC yield has also been examined for these homogeneous reactor simulations. Figure 3 presents isopleths of constant CO yield for three different dilution levels. Generally, apart from the NTC region, dilution is observed to have very little influence on the CO and UHC yield. Accordingly, we anticipate that dilution will have the greatest impact on those regions where the temperature is held low by large heat losses—typically in the squish and crevice regions. For mixture temperatures above about 1450 K, Fig. 3 indicates that the CO yield is hardly impacted by dilution. For temperatures above this threshold, combustion will

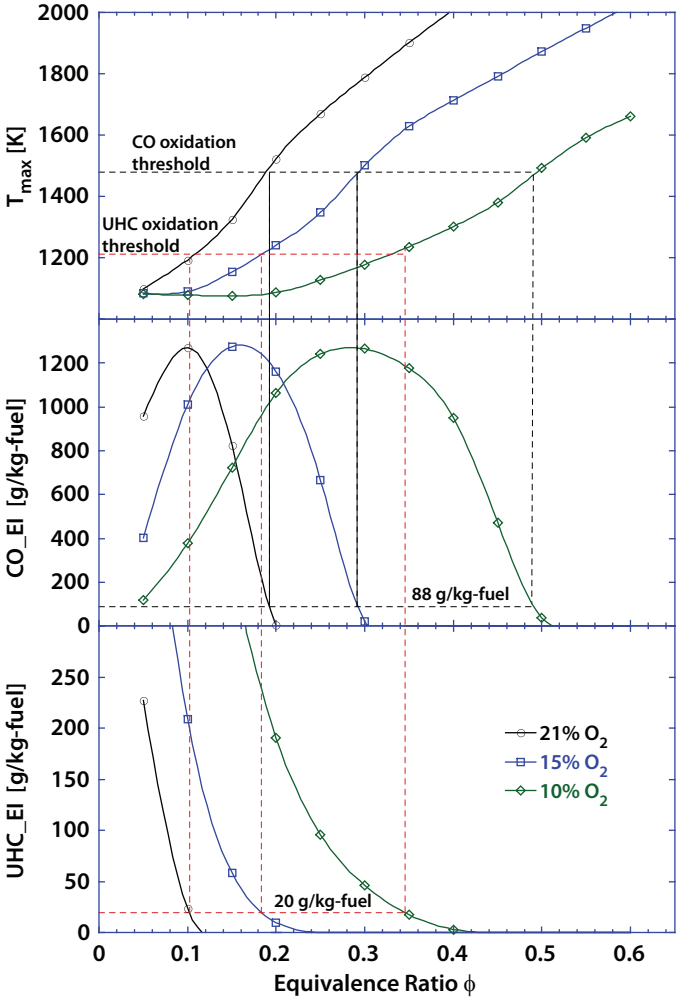

Figure 4 The maximum temperature achieved as a function of mixture equivalence ratio for various levels of intake charge dilution. Also shown are the CO and UHC yields

likely be completed on engine time scales even for highly dilute mixtures.

A significant shortcoming of these constant temperature and pressure simulations, however, is the artificial specification of the temperature. For lean, dilute mixtures the peak combustion temperature may never reach the threshold temperature required for complete, rapid oxidation to occur. A more realistic examination of the impact of dilution on oxidation processes was obtained by constraining the pressure to match the pressure trace measured at a typical, baseline operating condition (defined below), and solving the adiabatic energy equation for the gas temperature as the reaction proceeds. Computations were started at SOI plus a 'mixing delay' of 9°CA. The initial mixture temperature varied with ϕ and was set to the temperature achieved when liquid fuel initially at 293 K is mixed adiabatically with the core gases at an estimated temperature of 920 K. The peak cycle temperatures achieved in these simulations, and the CO and UHC yields at 90°CA[†]

[†] Positive crank angles cited in this paper correspond to °CA aTDC combustion; negative crank angles are bTDC.

Table 1. Engine and Fuel Injection Equipment Specifications

Engine	
Bore	82.0 [mm]
Stroke	90.4 [mm]
Displacement Volume	0.477 [L]
Effective CR	14.0
Squish Height	0.78 [mm]
Valve Events (0.15 mm lift)	
IVO	-359 °CA
IVC	-152 °CA
EVO	132 °CA
EVC	360 °CA
Fuel Injection	
Bosch Common Rail CRI2.2	
Rail Pressure	860 [bar]
Included Angle	149°
Number of Holes	7
Sac Volume	0.12 [mm^3]
Nozzle Hole Diameter	0.14 [mm]
Bosch Flow No.	440 [cm^3/30 s]
Fuel	US #2 Diesel

(when oxidation has effectively ceased), are shown in Fig. 4.

Several observations should be made from Fig. 4. First, even with no dilution, the peak adiabatic combustion temperature can be significantly lower than the temperatures considered in Figs. 1–3. Simulation results obtained at higher temperatures must therefore be discounted. Second, the temperatures required to rapidly oxidize CO and UHC are almost unaffected by dilution—as was seen previously in the constant temperature and pressure results of Fig. 3. However, an increase in dilution increases the equivalence ratio needed to achieve the required temperature and this temperature may not be achieved for dilute, lean mixtures. Finally, the peak cycle temperatures that result in near complete oxidation of CO and UHC correlate closely with those found in the constant temperature and pressure simulations. The required temperature for near complete CO oxidation is only slightly higher than seen in Fig. 3, and agrees well with the 1500 K limit cited in [10]. For near complete UHC oxidation, a temperature of roughly 1200 K is needed.

EXPERIMENT

ENGINE FACILITY

The optically-accessible single-cylinder research engine is derived from a 4-cylinder General Motors 1.9L light-duty diesel engine, which has the geometry and design valve events summarized in Table 1. Although the calculated geometric compression ratio (based on the full swept volume and measured TDC volumes) is 16.7,

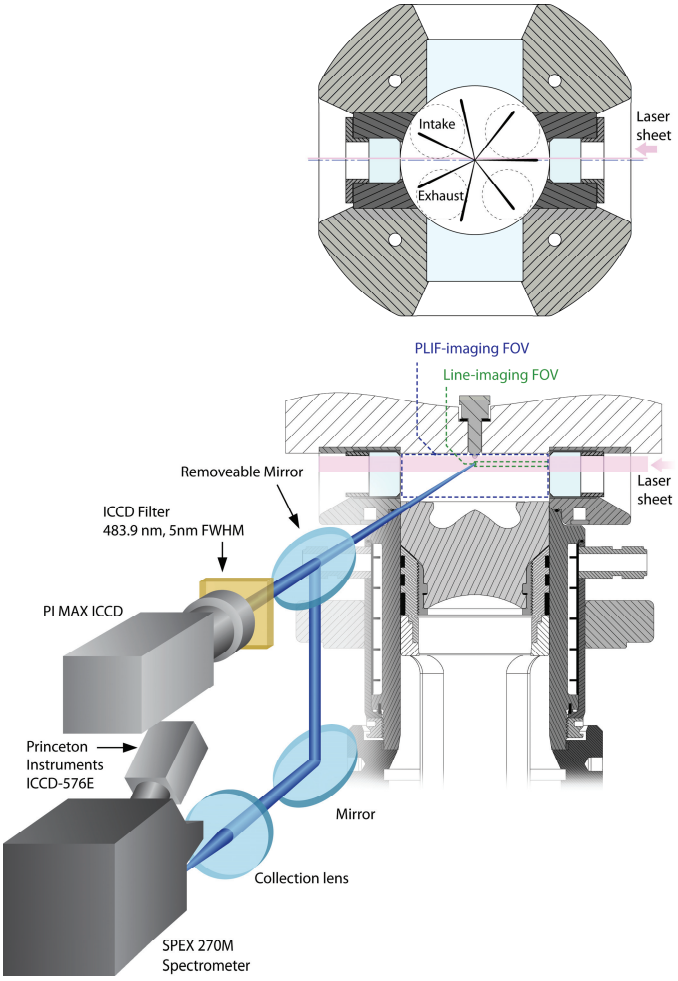

Figure 5 Cross-section of the optical engine and schematic representation of the experimental set-ups for 2-d PLIF imaging and 1-d spectrally-resolved imaging

a somewhat lower value of 14.0 is required to match the measured cylinder pressures using a one-dimensional model (WAVE 7.1), and better characterizes several aspects of the combustion behavior [17].

Table 1 also provides details of the fuel injection equipment, which incorporates a vertical, solenoid-actuated fuel injector, centrally located within the combustion chamber. The fuel employed was a typical US #2 diesel fuel, with a cetane number of 43.

The optical engine preserves the design bowl geometry, the piston top valve cut-outs, and the details of the head crevices. A geometrically-accurate representation of the bowl geometry is provided in Fig. 5. To maintain optical access from the side, the ring pack is positioned lower than on a conventional all-metal test engine. The top ring-land crevice has a height of 29.6 mm and width of 0.18 mm, and is the only significant geometrical deviation from a typical test engine.

OPERATING CONDITIONS

Data were acquired at an engine speed of 1500 RPM, at light loads where CO and UHC emissions are most

problematic. The performance and emissions behavior of this engine has been previously mapped for a wide range of intake O_2 concentrations, injection timings, and intake pressures [18]. From these measurements, a baseline 3 bar load operating condition typical of PPCI combustion was selected—with an intake O_2 concentration of 10% and an intake pressure of 1.5 bar. At this condition, the combustion efficiency at MBT timing is still acceptable (97–98%), but CO and UHC emissions have already increased significantly over the emissions levels observed at higher O_2 concentrations. The injection pressure was selected to match the pressure used for the previous emissions measurements. Around this baseline condition, the load was varied by ±1.5 bar, the O_2 concentration was varied from 9–15%, and injection timings both retarded and advanced from MBT timing were investigated.

To achieve the desired [O_2] concentration, the intake charge was diluted with additional N_2 and CO_2, with proportions selected to match the specific heat ratio (at 600 K) of the products of complete combustion. The total inlet mass flow rate was held constant at all operating conditions to maintain a constant TDC density. Because the intake temperature was fixed, the compressed gas temperature near TDC varied with O_2 concentration due to the changing mixture specific heat ratio associated with the increased dilution. The various operating conditions employed, and details of the intake charge composition, are summarized in Table 2.

OPTICAL ENGINE VALIDATION

To ensure that the in-cylinder combustion and emissions processes visualized in an optical engine are realistic representations of the processes that take place in a conventional engine, it is necessary to match not only geometry, but also the detailed operating conditions. This can be particularly crucial when attempting to acquire information on emissions, which may be quite sensitive to factors such as the in-cylinder surface temperatures. In practice, neither the geometry nor the precise operating conditions can be exactly reproduced. As noted above, differences will exist in details of the geometry and compression ratio, as well as in surface temperatures and intake charge composition (due to the necessity to simulate the EGR stream). Nevertheless, a comparison of combustion performance and emissions between this engine and a nearly identical all-metal test engine at a similar PPCI operating condition showed remarkable agreement in metrics characterizing the combustion process as well as in engine-out emissions [17]. In particular, CO and UHC emissions trends were very well captured, while a good quantitative agreement in magnitude was also obtained. The simplified EGR composition employed in this study was also shown to result in nearly identical combustion and emissions behavior as a more complex composition diluted with N_2, CO_2, H_2O, CO, and C_3H_8. Overall, the dominant processes influencing engine-out CO and UHC emissions appear to be well-represented in the optical engine.

Table 2. Operating conditions and charge composition

Speed	1500	[rpm]
Load	1.5 – **3.0** – 4.5	[bar]
Intake [O_2]	9.0 – **10.0**–15.0	[%]
SOI (command)	(-31.1) – (**-26.6**) – (-15.8)	[° ATDC]
T_{intake}	95	[°C]
P_{intake}	1.5	[bar]

Bold text indicates the baseline operating condition

Mole Fraction O_2 [%]	Intake charge mass fraction		
	Air	N_2	CO_2
0.09	0.413	0.437	0.150
0.10	0.460	0.402	0.138
0.15	0.701	0.222	0.077

LIF SET-UP AND DATA ACQUISITION

The experimental set-up employed for LIF imaging is also depicted in Fig. 5. CO and UHC fluorescence was excited using a UV laser beam generated by an injection-seeded Nd-YAG laser (Spectra-Physics Pro-290) pumping an optical parametric oscillator (Spectra-Physics MOPO 730) tuned to the desired wavelength. The laser beam was formed into a sheet using a single cylindrical lens with a focal length of 1000 mm. The resulting laser sheet had a height of approximately 7 mm and an estimated thickness of 0.4–0.5 mm. The energy delivered to the engine cylinder was typically 15 mJ per pulse, and was monitored on a single pulse basis using a pyroelectric detector (Coherent J4-09). With a characteristic pulse width of 4 ns, this corresponds to irradiance levels of about 1 x 10^8 W/cm^2.

The laser sheet was admitted to the engine through side windows in the cylinder liner. To minimize interference from fluorescence from the injector tip, the sheet centerline traversed a chord approximately 1 mm behind the cylinder diameter that is perpendicular to the viewing direction. Due to the high laser irradiance required, the inner surface of the windows etched rapidly, limiting the usable window life to just a few thousand laser shots. Although a laser shutter was installed to prevent the laser from striking the window unless a measurement was in progress, it was nonetheless necessary to replace the large liner windows with metal blanks that accepted smaller, more economical cylindrical windows having a clear aperture of 20 mm. This aperture limited the region of the cylinder illuminated to locations 3 mm from the head surface and below. To avoid laser damage to costly quartz pistons, the measurements were conducted with a titanium piston crown installed. Consequently, the measurement region was also limited to locations above the piston crown.

Fluorescent emissions were collected in the two distinct experimental configurations shown in Fig. 5. One configuration employed an imaging spectrometer to

provide spatial information in one dimension with spectral information characterizing the signal at each spatial location. The other provided 2-d spatial information (planar, or PLIF images). Details of these two configurations and processing of the images acquired are described below.

LIF images at each operating condition, crank angle, and laser wavelength (on-line or off-line) were acquired in separate tests in order to limit the engine operating time. A skip-fired strategy with fuel injection occurring once every five cycles was used. To ensure that the thermal state of the engine was the same for each test, a strict operating schedule was followed. Each test commenced with 90 s of motored engine operation, which allowed the intake plenum pressure to stabilize and the combustion chamber surfaces to preheat. This period was followed by 30 s of skip-fired operation, followed by acquisition of a background image set obtained with the laser sheet blocked. The background image set captures contributions from the camera fixed pattern noise and from natural combustion luminosity. Immediately following the background set, the LIF image set was acquired. After completing the LIF image set, the engine was stopped and allowed to cool for 5 minutes before repeating the test procedure for the next data set. Following this procedure resulted in good repeatability of the in-cylinder pressure traces and heat release phasing and magnitude.

Image sets were acquired at crank angles of 25, 30, 40, and 50°CA for PLIF and 30, 40, 50, 90, 170, and 320°CA for the spectrally-resolved, 1-d measurements. These crank angles were selected to capture the evolution of the CO and UHC distributions within the imaged volume (above the piston crown) as early as possible during the expansion stroke. The remaining crank angles were selected to capture the mean spatial distribution in the upper portion of the cylinder later in the expansion stroke (but before EVO), near the end of the blowdown process (but before reverse flow through the exhaust valve commences) and late in the exhaust process. The 1-d images acquired at the last two crank angles are obtained under conditions of nearly equal pressures and temperatures, as well as roughly homogeneous compositions. Likewise, beam absorption is minimal. Hence, despite the difficulties inherent in quantifying the CO and UHC LIF number density discussed below, these images can be quantitatively compared to examine the coarse axial distribution of CO and UHC within the cylinder during the exhaust stroke.

Cylinder pressure data were also acquired using a Kistler 6125B quartz pressure transducer, mounted in the production glow plug position. The data were acquired concurrently with the LIF images, at a resolution of 0.25°CA.

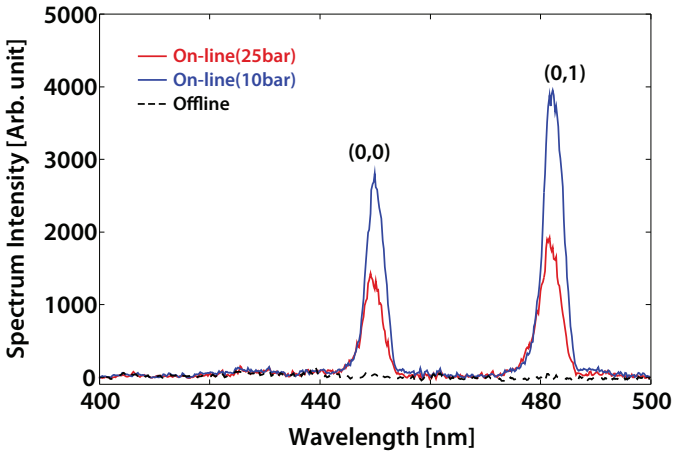

Figure 6 Sample emission spectra obtained with the laser tuned on and off the CO absorption band. Due to vignetting by the piston top at the higher pressure, no significance should be attached to the relative signal magnitudes

LIF DIAGNOSTIC DETAILS AND DATA ANALYSIS

CO

The CO LIF diagnostic is based on the two photon excitation of the $B^1\Sigma^+ \leftarrow X^1\Sigma^+$ (0,0) transition using laser radiation near 230.1 nm, with detection of emissions in the $B^1\Sigma^+ \rightarrow A^1\Pi$ system lying between 440 and 730 nm. This diagnostic has been applied in a number of combustion studies [*e.g.* 19,20,21], where additional spectroscopic details can be found. While the diagnostic has been shown to be applicable to flames characterized by appreciable soot concentrations [22], its application to engine flows has, to date, been limited to non-sooting SI engine studies [23] operating with unconventional (non-fluorescing) fuels.

The precise laser wavelength needed for the CO LIF measurements was found by performing excitation scans at atmospheric conditions and at pressures of 10 and 25 bar in the motored engine, with 5000 ppm of CO seeded into the intake stream. No significant shift in the wavelength yielding the peak fluorescence signal was observed at the higher pressures, though a significantly larger change in wavelength was required to eliminate CO excitation. Accordingly, the off-line excitation wavelength selected was red-shifted by 0.09 nm from the on-line wavelength. Examples of on-line and off-line emission spectra, obtained with the 1-d imaging set-up described below, are shown in Fig. 6.

Several distinct challenges exist in applying the CO LIF diagnostic to diesel engine combustion. Because it is a two-photon process, and because collisional quenching of the excited state is the dominant loss mechanism at high engine pressures, the high-pressure fluorescent signal is theoretically dependent on the square of the laser irradiance I. To maximize the CO signal, high laser irradiance is required, which is achieved by maximizing the laser energy and focusing the beam into a sheet with

a relatively small cross-sectional area. The I^2 signal dependency also requires that the sheet cross-sectional area be kept as constant as possible to maintain a spatially-uniform response. Consequently, irradiance levels at the cylinder walls are comparable to those at the cylinder centerline, and—as noted above—the windows in the cylinder liner through which the beam passes are rapidly damaged.

A second difficulty is associated with interference from fluorescent emissions from other species, notably UHC. Although spatial locations and operating conditions can be found at which interference from UHC is minimal, CO is often found co-located with UHC. To separate the CO signal from the UHC interference, images obtained with the laser tuned to the CO absorption line must be contrasted with off-line images obtained with the laser tuned to a nearby wavelength at which CO does not absorb. In the absence of a dual laser system, well-converged mean images are required for this on-line vs. off-line image comparison. Alternatively, as will be seen below, if signal spectral information is available spanning the CO emission wavelengths, the contribution to the signal from CO can be reasonably deduced. Under these circumstances, instantaneous CO signals can be obtained even with a single laser system, albeit with spatial information in only a single direction. It is noteworthy that high laser irradiance is helpful to extract the CO signal from UHC interference at high pressures. While the CO is expected to grow approximately as I^2, the UHC signal is observed to be considerably less dependent on laser energy—perhaps as a result of partial saturation.

Quantification of the CO signal level in terms of the number density of CO molecules is severely complicated by the following factors:

- The signal is highly dependent on irradiance, as noted above. This drawback can be partially overcome with careful monitoring of laser power and beam structure. However at lower pressures (after EVO), photo-ionization losses become comparable to quenching losses and the signal irradiance dependency will be influenced by the relative magnitude of these losses. Beam steering and de-focusing by in-cylinder refractive index gradients may add further uncertainty.

- The laser beam is strongly attenuated through absorption by unburned hydrocarbons under some conditions. The amount of absorption will change with the amount and composition of UHC present in the beam path.

- At a fixed mole fraction of CO, pressure will influence the signal by increasing the molecular number density and by increasing the collisional quenching rate. To first order, these effects cancel and the remaining influence of pressure is confined to line-broadening effects. Calculations of the magnitude of the pressure-broadened absorption spectrum indicate that, in the 800–1600 K temperature range, a five-fold increase in pressure from 10 to 50 bar approximately halves the two-photon absorption rate.

- Temperature variations will influence the ground state CO population distribution, also leading to changes in the absorption rate. At a pressure of 30 bar, an increase in temperature from 800 to 1600 K reduces the pressure broadened absorption rate at the laser excitation frequency by 14%.

- Temperature also impacts the number density, along with the collisional cross-sections and the collisional frequency—thereby influencing quenching rates. Quenching rates are also impacted by gas composition. To estimate the joint impact of temperature and composition changes on quenching rates, we have employed the results of homogeneous reactor simulations (described in the context of Fig. 4) of the combustion process for equivalence ratios ranging from 0.2 to 4.0. These simulations provide gas temperature, pressure, and composition histories, from which quenching rates are estimated using temperature-dependent quenching cross-sections [24]. For a fixed mole fraction of CO and a constant CO absorption rate, the signal is proportional to the number density divided by the quenching rate. This quantity is found to vary by approximately 25% over the full range of equivalence ratios during the expansion stroke. The influence of temperature on number density is the dominating factor, and the highest signals are expected for the richest and the leanest conditions, while a near stoichiometric mixture provides the lowest signal. It must be recalled, however, that these estimates neglect the potential impact of unburned hydrocarbons of unknown composition on the quenching rates. In general, quenching from these species can be expected to reduce the signals from the richest and leanest mixtures.

- CO may be photolytically produced from vibrationally excited CO_2. Data from Nefedov, et al. [25] suggest that at 2000 K, 2–3% of CO_2 molecules may be dissociated, potentially resulting in as much as 3000 ppm CO for the conditions considered here. As will be shown below, CO signals obtained at higher engine loads, resulting in both greater CO_2 concentrations as well as higher temperatures, are considerably lower than signals obtained at low loads. Photolytic production is thus not as pronounced as the above estimate suggests, and is unlikely to confuse a qualitative interpretation of the data. Richter, et al. [23] reach a similar conclusion.

For the above reasons, the CO fluorescent intensity cannot be quantitatively interpreted as being proportional to CO number density. The joint impact of temperature and composition on absorption rate, number density, and quenching by major species introduces uncertainties of approximately 40% at a pressure of 30 bar. Beam absorption, laser irradiance

dependency, and possible quenching by UHCs introduce additional uncertainties. Nevertheless, keeping these uncertainties in mind, CO LIF images can provide useful qualitative information on the in-cylinder spatial distribution of CO.

UHC

LIF measurement of UHC corresponds to fluorescent emissions observed when the laser is tuned off the CO absorption line. Spectral analysis of the off-line signals indicates that the bulk of the signal has characteristics typical of broadband PAH fluorescence [26], exhibiting the highest intensity at shorter wavelengths and decaying as wavelength increased. Superimposed on this broadband background are spectral features characteristic of the CH $A^2\Delta \rightarrow X^2\Pi$ system (near 430 nm) and the C_2 $d^3\Pi \rightarrow a^3\Pi$ Swan bands (near 438, 470, and 513 nm). These features are not always present, and may prove to be of diagnostic value. As explained in greater detail below, when spectral information is available from 1-d images, the entire spectrum, less the contributions from CO, is integrated to obtain the UHC signal. For 2-d images, obtained with a bandpass optical filter, the UHC signal is dominated by the broadband PAH background, though there is some contribution from C_2 fluorescence as well.

Although the experiments described below suggest that the UHC fluorescence is relatively insensitive to laser irradiance, quantification of the UHC signal is not possible due to the unknown composition of the fluorescing species. However, under conditions of approximately equal pressures, temperatures, and compositions we believe that, like the CO fluorescent images, the UHC images can be cautiously interpreted as a qualitative representation of the spatial distribution of UHC.

SPECTRALLY-RESOLVED, 1-D IMAGING

As shown in Fig. 5, fluorescent emissions employed for spectrally-resolved, 1-d imaging are collected from a portion of the beam spanning the distance from the cylinder centerline to the bore wall, and are focused onto the entrance slit of an *f*/4, 1/4-meter imaging spectrograph (Spex 270M). The imaging is performed with a horizontal (spatial) axis magnification of approximately 1/6—a value that accounts for the distortion caused by the cylinder liner window. The low magnification was required to allow the full cylinder radius to be imaged onto the CCD detector at the exit plane of the spectrograph, but it adversely impacts the collection solid-angle that can be employed and consequently the signal level. For this reason, and due to the expectation of approximately axisymmetric CO and UHC fields during the expansion stroke, only ½ of the cylinder bore was imaged. In the vertical direction, the magnification is approximately 1/4.8. With the entrance slit width set to 0.5 mm, light was therefore collected from a 2.4 mm high segment of the laser sheet centered 6.0 mm below the piston head.

The spectrograph was fitted with a 400 groove/mm grating, providing a spectral dispersion at the exit plane of 8.8 nm/mm. With a 0.5 mm entrance slit width, a spectrograph magnification of 1.2, and a detector width in the exit plane of 13.25 mm, the system can resolve spectral features separated by about 5.3 nm and each image covers a bandwidth of 116 nm. For the fixed grating angle used, the wavelengths covered ranged from 394–510 nm. The wavelength calibration of the spectrograph was based on a 2nd order polynomial fit to 6 spectral lines from Ne and Hg-Ne calibration lamps.

The detector was a gated, 384 x 576 pixel ICCD (Princeton Instruments ICCD-576E) controlled by a Princeton Instruments ST-138 controller and a PG-200 high-voltage pulser. The larger detector dimension was aligned with the wavelength axis. The gate width was set to 70 ns and timed to maximize the signal obtained. Due to the low-magnification collection optics, signal strengths were low and single-cycle images were not feasible. Consequently, mean images corresponding to 50 engine cycles were integrated on-chip, employing the maximum intensifier gain.

A sample image of CO and UHC fluorescence, taken in the operating engine, is depicted in the lower portion of Fig. 7. To aid in its interpretation, Fig. 7(a) shows an image of a calibration target obtained with the grating angle set to zero wavelength (where the grating functions as a mirror) and with the slit fully open. From these images it is apparent that spatial information is conveyed by the vertical image axis; the horizontal image axis conveys the spectral information. The calibration target image is employed to define vertical strips of height 3 mm (about 27 pixels). Spectra characteristic of each strip are generated by summing the pixels vertically in each strip. This spatial calibration thus accounts for the image distortion caused by the curved liner window. A grating rocking adjustment was performed to ensure that the spatial calibration was not influenced by the grating angle.

Typical binned spectra, derived from the on-line image of Fig. 7(b), are shown in Fig. 8. The strip number on the upper left-hand side indicates the spatial location of each spectrum and corresponds to the labels on the right-hand side of Fig. 7(a). As discussed previously, in addition to the two CO transitions the spectrum contains a broadband contribution due to PAH fluorescence, as well as additional peaks associated with the C_2 Swan system and a peak near 430 nm consistent with CH fluorescence. Nevertheless, the contributions from CO can be spectrally-separated from all but the broadband PAH background. With minor exceptions at higher load and retarded SOI, no contribution to the background signal from broadband, blackbody-like soot luminosity was observed.

Also shown in Fig. 8 are off-line spectra obtained at the same operating condition. Identification of the CO signal is unambiguous at all locations. However, a close comparison of the on-line and off-line spectra reveals

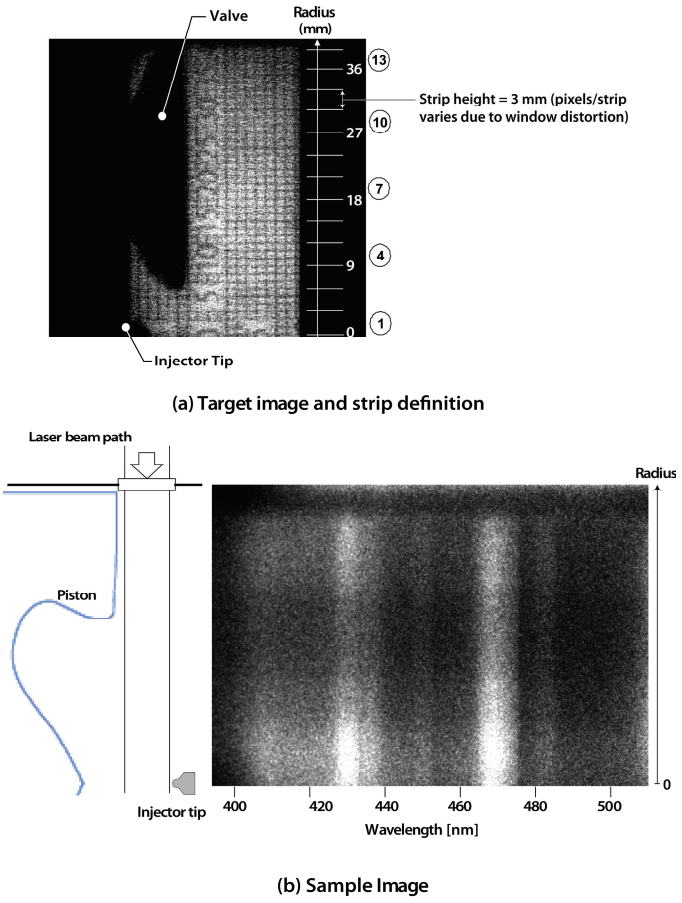

Figure 7 A sample image obtained through the spectrograph and the spatial calibration image employed to define the spatial strips. Baseline operating condition, 90°CA

subtle differences in their shape, even in regions away from the CO transitions. We believe these differences are due primarily to insufficient convergence of the mean image, based on the limited number of cycles employed. The repeatability of the operating conditions from test-to-test is a second possible factor.

Differences in the shape of the spectra create difficulties in determining the appropriate background level to subtract prior to integration of the CO transition signals. Appropriate scaling of the off-line spectrum can seem to vary from one wavelength region to another and from bin to bin. Locally scaling the off-line signal to match the on-line signal is not always an effective solution, as the off-line signal on either side of a CO transition can scale differently. An example of this behavior can be seen near 480 nm in the spectrum derived from strip #10.

To overcome these difficulties, the background level was estimated directly from the on-line spectra. For each of the CO transitions, several pixels on either edge of the transition were selected and averaged. The representative background intensity for each transition was then chosen to be the smaller of the two averages. Examples of the background levels determined in this manner, and the delineation of integration regions selected for analysis of the two CO transitions, are also shown in Fig. 8. The choice of this method was made by

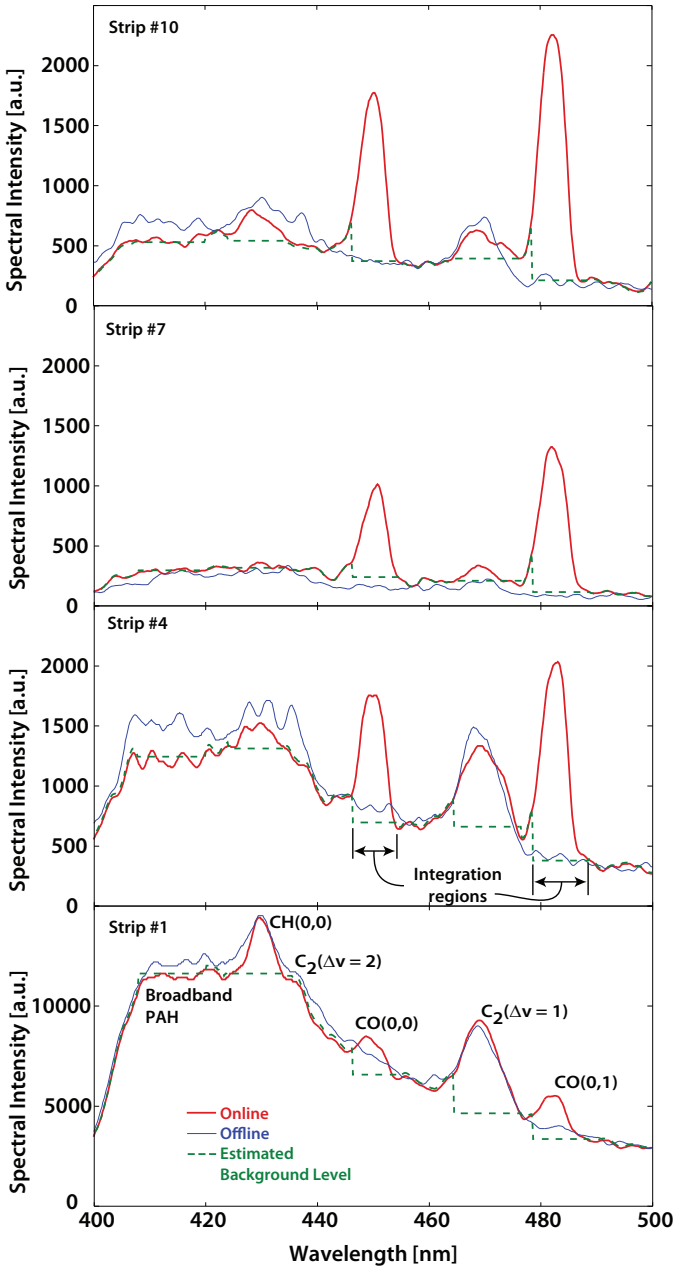

Figure 8 Sample spectra comparing the signals obtained with the laser tuned on and off the CO absorption band and showing the estimated background levels subtracted before integrating the CO transition peaks

comparing the resulting background levels with a subjective assessment of the behavior of the off-line spectra in the vicinity of each transition. If the representative background level were chosen to be the average of the intensity on either side of the transition, the background level would typically be overestimated due to the overlap of signals obtained from C_2 or CH transitions.

The difference between CO signal estimates obtained with the above procedure and estimates obtained by subtracting a scaled, off-line spectrum was generally far less than the uncertainties introduced by beam absorption or estimated variations in the local quenching

rate. However, in regions with low CO concentrations and at higher pressures—where signal levels were low—the procedure chosen gave more consistent results resulting in a smoother spatial variation.

For both the CO and UHC signals, a systematic decrease in the intensity of the light imaged through the spectrograph was observed as the cylinder wall was approached. The loss of signal was only severe ($\approx 40\%$) for the bin closest to the cylinder wall. This decrease was due mainly to spatial variations in the optical efficiency of the imaging system. To compensate for this variation, the CO signals obtained in a homogeneously seeded motored flow were analyzed at various pressures and averaged to yield a typical spatial response function. The response function was used to normalize the CO signal spatial profiles obtained with the engine firing. Besides correcting for spatial variations in the imaging system efficiency, this normalization also compensates for mean spatial variations in the laser sheet irradiance. For the UHC signals no images of a homogeneous UHC field were available, and a similar correction could not be made.

In addition to variations in the spatial response function, fluorescence from the window through which the laser sheet enters the cylinder impacts the UHC signal near the cylinder wall. With standard grade (Corning 7980) fused silica windows, significant fluorescence was observed from the window material. Approximately midway through the measurement program, ArF grade beam entrance windows were installed to minimize potential interference from this source. However, fluorescence from contaminants on the window surface can still introduce an interfering background signal. The bulk of the window fluorescence is observed at radii greater than 39 mm, and only a small amount impacts the UHC signal found in the outermost spatial strip (#13). Despite this interference, the UHC signal levels reported near the wall are likely underestimated due to the decreasing spatial response function.

In consideration of the above discussion, analysis of the one-dimensional images proceeded as follows:

1) Background images were subtracted from the on-line and off-line images obtained at each operating condition and crank angle. The background was always dominated by fixed pattern noise; natural combustion luminosity could rarely be detected.

2) A 3 x 3 median filter was applied to eliminate “hot” pixels, without significantly smoothing the data. This was followed by a 12 x 12 Gaussian smoothing filter. The characteristic filter width, $\sigma = 4.8$, corresponded to about 1 nm along the spectral axis and 0.5 mm along the spatial axis.

3) Representative spectra corresponding to spatial regions 3 mm wide were computed. An appropriate background level was determined for each CO transition, and validated by visual comparison with spectra computed from the off-line images.

4) CO signals were computed by integrating the on-line spectra (less the background) over both CO transitions. The resulting spatial profiles were corrected for the system optical response, and further normalized by the square of the mean on-line laser energy.

5) UHC signals were computed from the integration of the full on-line spectrum, less the signals corresponding to the CO transitions. UHC spatial profiles were normalized by the mean on-line laser energy. This normalization assumes that the UHC fluorescent emissions are linearly related to laser irradiance, although evidence given below suggests that the fluorescence may be partially saturated. Because mean laser energies varied by only ±6% ($\pm 1\sigma$), the validity of this assumption is of little practical consequence.

6) The spatial profiles are presented normalized by the maximum signal value measured at each crank angle for the operating conditions shown in the figure. This allows a comparison of the relative magnitude of the signals obtained at a fixed crank angle as SOI, load, or dilution levels are varied. The uncertainties discussed above must be kept in mind, however.

   The normalization process does not allow a comparison of signal levels at different crank angles to be made. As the crank angle varies, simultaneous changes in pressure and temperature create larger uncertainties, and such a comparison would be of dubious value. An exception is made for data obtained during the exhaust stroke, when the cylinder pressure (and temperature) is approximately equal at both 170 and 320°CA. In this case, the signals obtained at both crank angles are normalized by the same value.

Two-dimensional imaging

Two-dimensional PLIF images were acquired collecting fluorescent emissions at 90° from the laser sheet, using a Nikkor 50 mm lens with an additional +4 diopter close-up lens fitted to a Roper Scientific PI-Max intensified camera with a resolution of 512 x 512 pixels. The camera was positioned so that the full cylinder bore filled the field of view and the lens aperture set to *f*/1.4. Like the one-dimensional images, the intensifier gate duration was 70 ns, timed to minimize signal clipping. A 50.4 mm diameter interference filter, placed at a 5° tilt angle to blue-shift the passband, was employed to reduce the UHC interference to acceptable levels while passing emissions due to the CO $B^1\Sigma^+ \rightarrow A^1\Pi$ (0,1) transition near 483 nm. Accounting for tilt, the filter was characterized by a FWHM of 5 nm and a center wavelength of 483.9 nm.

The filter passed not only broadband UHC fluorescence associated with PAHs, but also some of the C_2 ($\Delta v = 1$) Swan band emissions. Although a tighter filter passband could be employed to further reduce interference from UHC, it is desirable to retain a reasonable fraction of the UHC signal if off-line images are to be a useful measure of UHC. Moreover, spectral analysis of the signals demonstrated that—for the majority of operating conditions—PAH emissions would remain significant and an off-line image subtraction methodology would still be required. Note that, due to the differences discussed earlier between the on-line and off-line signals, an off-line background subtraction scheme will likely suffer from greater inaccuracy than the background subtraction made possible with the full spectral information available in the 1-d images.

The intensity of single-cycle images, typically having a 500 count maximum at an intensifier gain of 35% of the maximum, was sufficient for single-cycle images to be acquired. However, because a corresponding off-line image could not be obtained on a single-cycle basis, only mean image sets, corresponding to 50 engine cycles, were acquired. These images were integrated on-chip to minimize extraneous noise.

The on-line, off-line, and corresponding background images were processed using the following steps:

1) The background image (dominated by fixed pattern noise), was subtracted from the corresponding on- or off-line image.

2) The back-ground corrected off-line image was normalized by the mean laser energy to yield a normalized UHC image.

3) The normalized UHC image was scaled by the mean laser power corresponding to the on-line image, and then subtracted from the background-corrected on-line image. The result was divided by the square of the mean on-line laser energy to compensate for the I^2 irradiance dependency of the CO fluorescent signal, yielding a normalized CO PLIF image.

4) The normalized UHC and CO images were lightly filtered by a 9 x 9 filter with a Gaussian kernel characterized by a standard deviation of 1.6 pixels (about 0.2 mm).

5) The filtered images were distortion corrected using a 2-dimensional cubic fit to the image of an orthogonal calibration grid of equally spaced points.

6) Final images are presented with the same intensity scale (effective gain) for images obtained at equal crank angles.

The laser sheet had stable, vertical spatial variations in mean irradiance, leading to irradiance-induced variations in the image intensity. Our efforts to compensate for these variations, by normalizing with images obtained in homogeneous CO concentration fields, added significant noise to the final images and suffered from difficulties near the edges of the laser beam that we felt could be misleading. Moreover, as mentioned earlier, at the lower pressures when quenching and photo-ionization losses become comparable the signal irradiance dependency will vary. In lieu of normalization, we provide in Fig. 9 a typical image obtained with CO seeded homogeneously into the cylinder to aid the reader in judging the influence of laser irradiance variations.

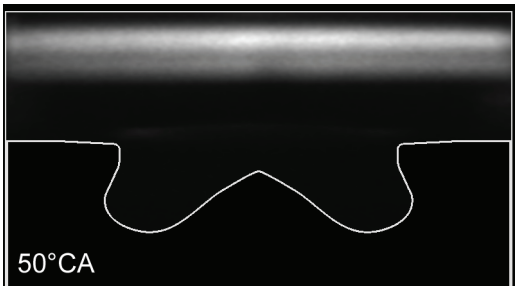

Figure 9 Image of a homogeneous field of CO within the cylinder obtained at a pressure of 1 bar

RESULTS

CYLINDER PRESSURE

Cylinder pressure traces typical of each operating condition are provided in Fig. 10. Our objective in providing these traces is twofold: First, the pressure traces allow the reader to gain a qualitative idea of how the combustion proceeds at this dilute operating condition and how changing SOI, oxygen concentration, and load impact the combustion process. Second, they illustrate the variation in pressure (and mean cylinder temperature) that occurs at the crank angles of the LIF measurements as these same parameters are varied. Generally, the pressure and mean cylinder temperature will be closely comparable for the SOI sweeps, with larger differences observed for the O_2 sweeps and the load sweeps. At 30°CA, the largest difference in pressure is 780 kPa (28% of the baseline pressure), observed as the engine load is varied.

EXPANSION STROKE LIF IMAGING

Two-dimensional images of the mean spatial distribution of CO and UHC fluorescence obtained during the expansion stroke are shown in Figs. 11 and 12, respectively. Images obtained at the two other injection timings investigated are also shown.

A first observation to make from the CO images is that on the left-hand side (LHS) of the cylinder there is very little CO fluorescence apparent. At these crank angles, 50°CA or more ASOI, we expect the spatial distributions of the various species to be nearly axisymmetric. The apparent absence of CO on the LHS is therefore likely to be mainly due to strong laser sheet absorption, coupled with the I^2 dependency of the CO LIF signal. In contrast,

the LHS of the UHC images show much less attenuation. If the bulk of the UHC fluorescence is associated with unsaturated single-photon absorption processes, the signal decrease would be less than seen in the CO images due to a linear dependency on irradiance. In some cases, however, the decrease is sufficiently small that we suspect partial saturation.

Two additional features of the UHC fluorescence images in Fig. 12 should be brought forward before discussing the results in detail. First, in many images a distinct oval region in seen adjacent to the head surface—this is due to fluorescence from semi-liquid fuel residue that can accumulate on the base of the injector nozzle. Second, the spatial extent of fluorescence from the windows and deposits on the window surfaces is well illustrated by fluorescence from the (standard grade fused silica) beam exit window. Note that this region is generally considerably smaller than the corresponding region of UHC fluorescence seen near the beam entrance window.

Although the images presented in Figs. 11 and 12 are useful for developing a qualitative, visual understanding of the species distributions, spatial information in the vertical direction is limited due to the small laser sheet height. This, and the absence of CO information on the LHS of the cylinder, means that much of the information conveyed is equivalent to that provided by the 1-d imaging experiments. Moreover, in the 1-d configuration, the additional spectral information available allows low CO signal levels to be extracted with greater confidence. To complement the 2-d images in Figs. 11 and 12, radial profiles of the CO and UHC signals obtained during the expansion stroke with the 1-d imaging configuration are presented in Fig. 13.

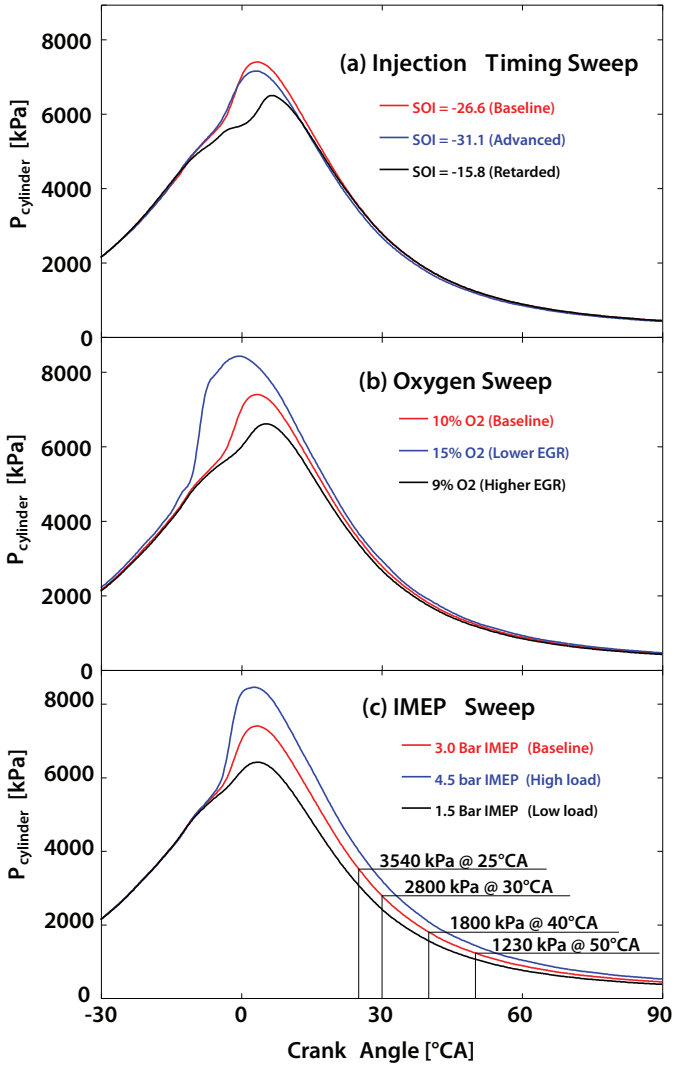

Figure 10 Cylinder pressure traces for each of the operating conditions investigated

Baseline operating condition

Focusing first on the baseline operating condition, Figs. 11-13 show that UHC fluorescence is predominantly detected in two locations: near the cylinder centerline and in the squish volume, close to the cylinder walls. The centerline UHC is reminiscent of the near-injector UHC observed in heavy-duty engines [27], which has been convincingly attributed to over-lean mixture that forms at the end of the injection event under conditions when the ignition delay is large [13]. This view appears to conflict with the traditional correlation of UHC with nozzle sac and hole volume [12], which suggests that an important source of UHC is fuel leaving the sac volume after the injection event and subsequently mixing poorly. Moreover, soot visualization studies in a similar, light-duty engine have clearly shown the presence of soot near the cylinder centerline during expansion [28]. Whether the UHC near the cylinder centerline stems from over-lean or over-rich mixture remains unclear. As will be seen below, much of the evidence gathered in this study is consistent with either situation.

Note that the centerline UHC cloud is initially quite localized, although over 50°CA have elapsed since the injection event. Mean velocity fields measured in similar engines with comparable operating conditions [29] exhibit a radially-inward flow near the nozzle beyond TDC. Such mean flows could be partially responsible for confining the UHC to the centerline region, though these flows persist well into expansion—while the UHC cloud appears to be spreading. Alternatively, the localized UHC cloud may be indicative of fuel leaking from the injector sac and hole volumes. Such leakage would not be expected to be significant until the cylinder pressure dropped below the pressure at EOI, which occurs near 25°CA. Neither the velocity measurements cited above nor multi-dimensional simulations [30] of similar engines suggest that the UHC cloud near the centerline is likely to be augmented from fluid transported up from the bowl region at these crank angles. Hence, we believe the radial expansion of the centerline UHC cloud observed as the stroke progresses is likely due primarily to turbulent diffusion.

UHC within the squish volume is generally concentrated close to the cylinder wall, suggesting that it emanates from the crevice region. Spray targeting estimates [18]

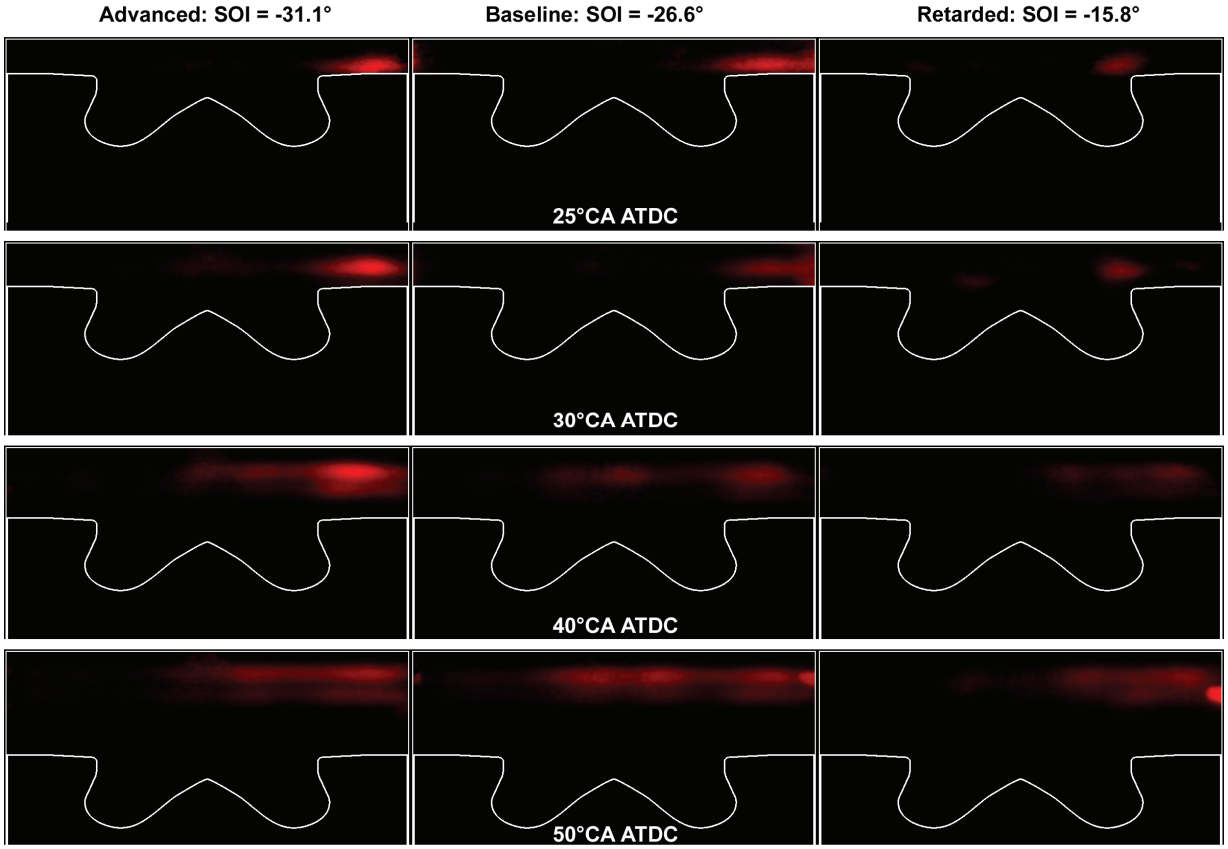

Figure 11 Evolution of the spatial distribution of CO during the expansion stroke as observed with the two-dimensional imaging set-up. The laser traverses the cylinder from right to left

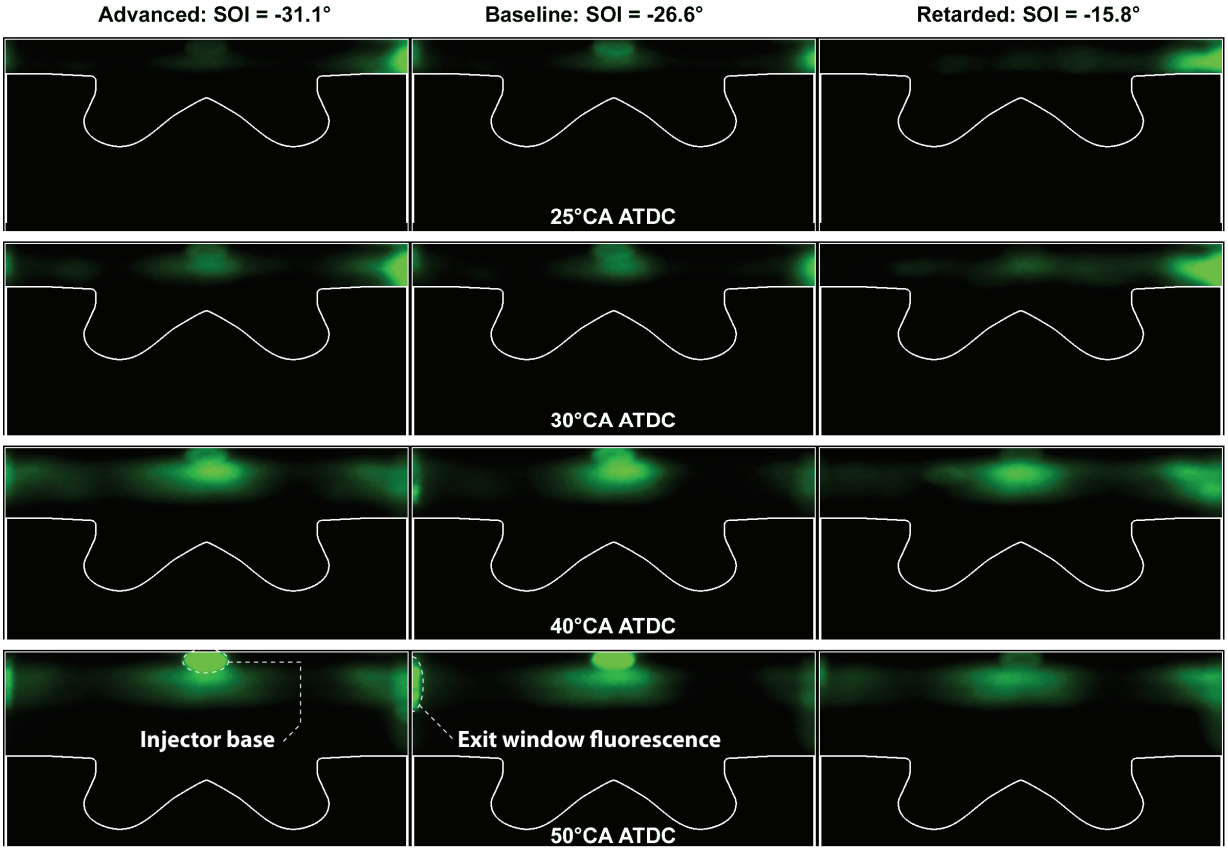

Figure 12 Evolution of the spatial distribution of UHC during the expansion stroke, corresponding to the CO distributions shown in Fig. 11

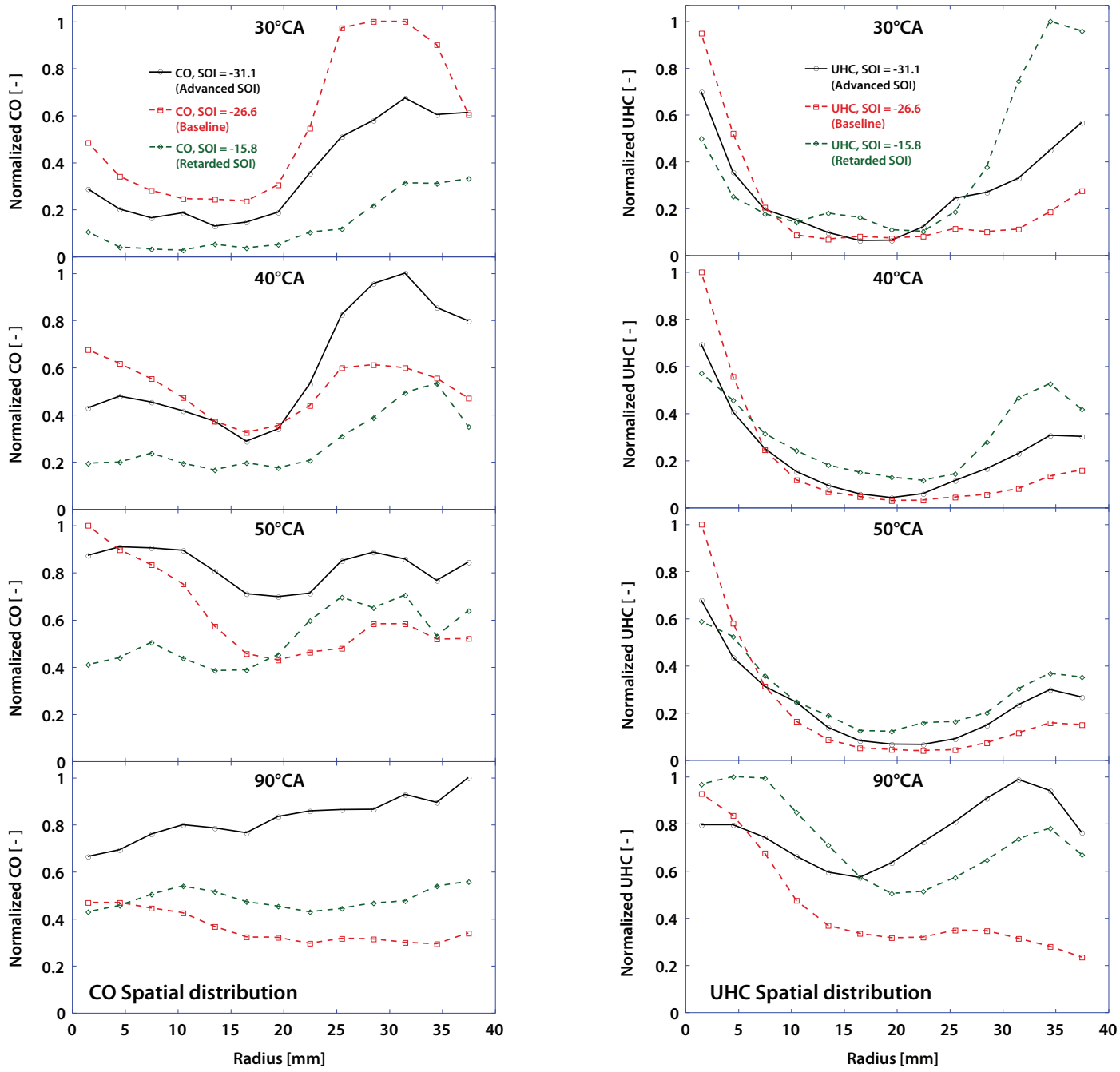

Figure 13 Spatial profiles of the CO and UHC signals derived from the one-dimensional imaging experiments, measured during the expansion stroke for three different injection timings

show that, at the baseline injection timing, liquid fuel is unlikely to penetrate into the squish volume or to impact the liner. However, significant fuel vapor is likely to be present in the squish volume, and to be compressed into the top ring-land crevice as the piston approaches TDC. Based on the CO distributions and the results of the load sweep presented below, we expect that this UHC observed near the cylinder walls stems from fuel-lean mixture.

UHC emissions stemming from ring-land crevices have been found to be unimportant in diesel combustion systems using fuel injectors with a narrow included angle [16]. These data clearly indicate that crevices are a potential source of UHC emissions in combustion systems with more conventional, wide-angle injector geometries. When weighted by the greater cylinder volume associated with the larger radii, the magnitude of the UHC signal near the cylinder wall is comparable to the signal arising from the centerline region. However, the reader must recall that even a semi-quantitative interpretation of the UHC signals could be misleading, and that the importance of crevice sources is likely to be exaggerated in the present study by the large top-ring land of the optical engine.

The spatial distribution of CO observed at the baseline condition differs from the UHC distribution in both the

central region of the cylinder and in the squish volume. Early in the expansion stroke, 25–30°CA, there is very little CO found near the cylinder centerline. Nevertheless, the radial profiles of Fig. 13, which more reliably show smaller CO signals, indicate that there is a local maximum near the cylinder centerline, similar to that seen in the UHC profiles. Laser sheet absorption likely reduces CO signals near the cylinder centerline. Hence, the local maximum in CO concentration may be larger than indicated by the signal levels.

As the expansion stroke progresses, CO near the centerline appears and spreads radially. Because the appearance of CO cannot be easily accounted for by mean flow transport, we believe it more likely stems from the gradual, delayed oxidation of UHC near the injector tip—either from lean mixtures formed at the end of the injection event or from richer mixtures formed when fuel leaves the injector as the cylinder pressure drops. Homogeneous reactor simulations indicate that for fuel leaving the injector at 25°CA (when the cylinder pressure is approximately equal to the pressure at EOI) even stoichiometric mixtures fail to oxidize the CO formed, and CO continues to be formed well beyond 50°CA for rich mixtures.

Unlike the centerline region, there is significant CO observed within the squish volume at 25–30°CA. Although the PLIF images of Fig. 11 occasionally show CO fluorescence at the cylinder wall, this is likely due to the large UHC background that must be subtracted at these locations. Spatial profiles of CO fluorescence obtained from the 1-d images (Fig. 13) clearly show that the CO signal peaks in the middle portion of the squish volume and decreases as the cylinder wall is approached. As discussed in the section describing the homogeneous reactor modeling, high CO in the absence of UHC will normally stem from either moderately rich mixtures ($1.0 \lesssim \phi \lesssim 1.3$) at relatively high temperature, or generally lean mixtures at temperatures between about 1200 and 1400 K. In this case, the latter source is more probable. Squish volume gases are subject to high heat losses while the piston is near TDC, and—in the absence of significant heat release—will only cool further as the gases expand. Evidence derived from the load sweeps presented below further suggests that the mixture in the squish volume is lean overall.

Near the cylinder wall, decreasing CO fluorescence is consistent with fluid emanating from the crevice is that is too cold and/or lean to react rapidly. Moreover, mixing of the cold fluid leaving the crevice with cool, lean squish volume gases could slow their combustion progress. Hence, CO may only be formed in higher temperature regions away from the wall.

At intermediate radii between 10 and 20 mm, both low CO and low UHC are initially observed. In this region, the mixture is either very lean, or—more likely—sufficiently close to stoichiometric to fully oxidize the fuel in the time available. In contrast to the centerline region, measured and computed flow structures in similar engines suggest that CO in this region (especially near the bowl lip) may be transported there with fluid arriving from lower in the cylinder.

SOI sweep

UHC fluorescence in the centerline region evolves similarly for all three injection timings, although with retarded injection considerably less UHC is observed at 25–30°CA—behavior that could be due to increased beam attenuation by UHC near the wall. Little can be determined from these results regarding the source of this UHC—whether it stems from over-lean or from poorly-mixed, over-rich regions. Likewise, with retarded injection less initial CO fluorescence is seen along the cylinder centerline, a situation which persists through 50°CA. Beyond 50°, centerline CO levels observed with advanced injection are comparable to or higher than the other cases, behavior which is observed at all radii and which will be shown below to correlate closely with engine-out CO emissions measured under similar operating conditions.

In the squish volume, spatial distributions of both UHC and CO fluorescence are altered significantly as SOI is varied. For both advanced and retarded SOI, UHC is more broadly distributed within the squish volume, indicating a source of UHC in addition to the near-wall source identified for the baseline case.

For advanced SOI, a strong case can be made that a rich mixture is formed within the squish volume, and is responsible for both the higher UHC and, eventually, the higher CO signals. Consider that:

- Compared with the baseline case, there is initially a greater amount of UHC in the squish volume, but less CO (Fig. 13[†]). This behavior could be caused by the formation of a leaner mixture with advanced injection. However, during the injection event the piston position is lower and lower ambient density results in more rapid spray penetration. Both of these factors increase the probability of putting fuel directly into the squish volume—including liquid fuel—when injection is advanced. Hence, formation of a richer mixture in the squish volume is far more likely.

- If advanced injection produced a richer, but still lean mixture, combustion in the squish volume would likely be enhanced, leading to lower UHC levels (*cf*. Fig. 4). At all crank angles, however, advanced SOI results in considerably higher UHC signals.

The remaining alternative, that an overall rich mixture is formed with advanced injection, is consistent with the behavior of both the UHC and CO fluorescence. The initially lower CO levels in the squish volume observed in Fig. 13 could be associated with delayed mixture

[†] In contrast to Fig. 13, Fig. 11 indicates higher CO signal levels at the earlier crank angles. This is one of the few inconsistencies observed between the results of the different imaging configurations.

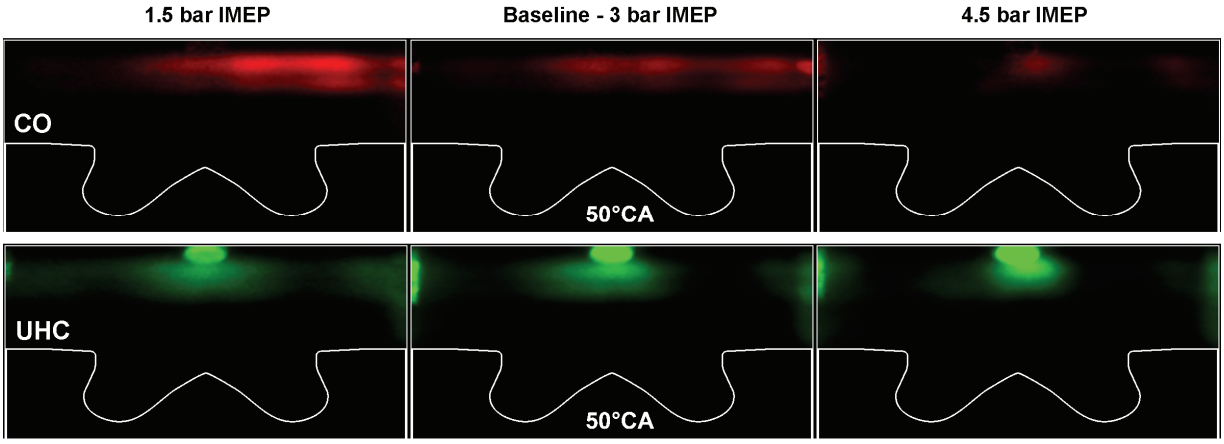

Figure 14 Two dimensional images of CO and UHC distributions obtained at the baseline 10% O_2 concentration at 50°CA

formation and combustion, as might be caused by the formation of liquid films. However, the UHC images of Fig. 12 do not show strong evidence supporting the existence of such films.

For retarded injection, a very different scenario is most plausible. Compared with the baseline timing, significantly higher UHC signals are observed in the squish volume at all crank angles. With retarded injection, less fuel is expected to be delivered to the squish volume, and the higher UHC is almost certainly due to formation of over-lean mixtures that, coupled with squish volume heat losses, result in slow combustion. The behavior of the CO signal, which is initially lower than the baseline case within the squish volume, further supports this view. As the cycle progresses, the CO levels increase, and eventually exceed the baseline timing levels. This behavior is consistent with the delayed oxidation of the squish volume UHC to CO for lean mixtures, followed by a slower oxidation of CO to CO_2.

The behavior described above is direct experimental confirmation of conclusions reached in previous studies [4,5] aimed at identifying the reasons for the existence of an optimal injection timing that minimizes fuel consumption, CO, and UHC emissions. Based on emissions trends, multi-dimensional simulations, and the predictions of phenomenological spray models, these studies also reasoned that increased CO and UHC emissions with advanced SOI were due to excessive fuel penetration into the squish region. However, the detrimental impact of lean mixture formation within the squish volume under more retarded injection timings was not previously identified.

Load sweep

Figure 14 shows two-dimensional images of CO and UHC fluorescence at 50°CA obtained at the three load conditions—each employing the same fixed, baseline injection timing. Likewise, radial spatial distributions of the CO and UHC signals, measured in the one-dimensional imaging configuration, are shown in Fig.15 for a broader range of crank angles.

Along the cylinder centerline, UHC signal levels are comparable for all three loads, though it is clear that by 50°CA the spatial distribution is more concentrated toward the cylinder centerline at the higher load. This suggests that mixing with higher temperature fluid from outside the centerline region, or higher compression temperatures near the centerline caused by higher peak pressures, has helped speed the oxidation of centerline UHC. In either case, this behavior provides evidence that the centerline UHC signal, at least at the lower loads, has contributions from over-lean mixture.

This conclusion is supported by the CO signals near the centerline at the lowest load, which Fig. 15 shows are decreasing as the centerline is approached, while the UHC is sharply increasing. The minimum in CO at the centerline is unlikely to be caused by beam absorption, since at the higher loads the UHC concentration is increasing more rapidly as the centerline is approached, yet the CO signal is increasing as well. Consequently, these counter-aligned gradients in CO and UHC fluorescence are probably indicative of temperature and equivalence ratio gradients caused by the presence of cooler, leaner mixture nearer the cylinder centerline.

Like the results observed with retarded SOI, at light load the UHC signal levels in the squish region are both higher and more spatially dispersed than at the baseline or higher load conditions. The light load CO signals are also highest. Again, this behavior is almost certainly due to incomplete combustion of lean mixtures at the modest temperatures prevailing in the squish volume. Despite uncertainties in quantifying the CO signal, CO emissions emanating from the squish volume will surely dominate over emissions stemming from the centerline region, an observation that is also pertinent to the higher loads. Note that while UHC levels in the centerline region are greater, the larger volume of fluid at the larger radii dominates, and squish volume UHCs are likely the more significant source of engine-out UHC at the lightest load.

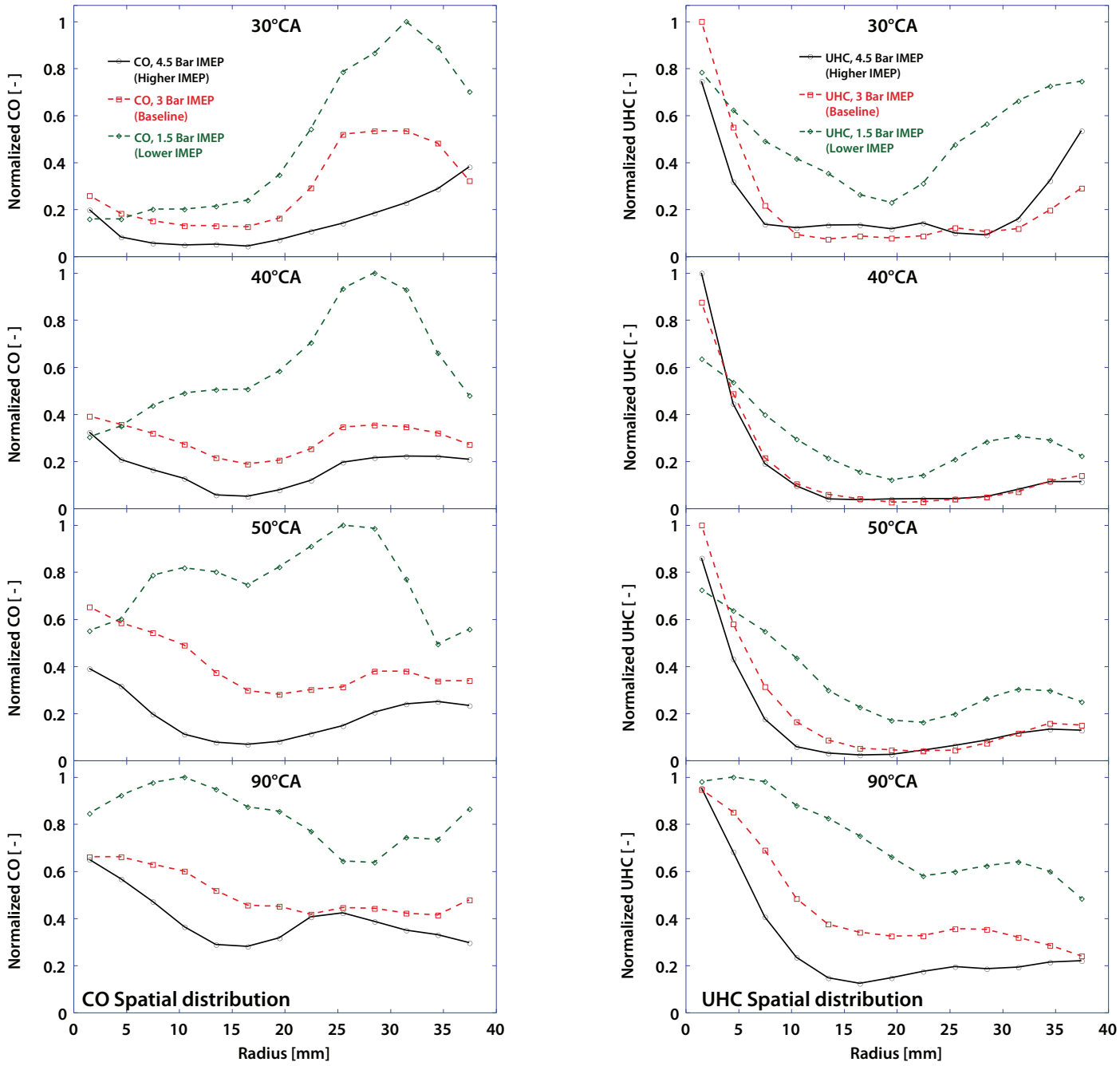

Figure 15 Spatial profiles of CO and UHC measured with the one-dimensional imaging technique as a function of engine load

At the highest load, higher UHC signals are seen near the cylinder wall at 30°CA. This may indicate a greater release of UHC from the ring-land crevice. Nonetheless, by 40°CA the squish volume UHC signals at the baseline and higher loads take nearly identical, low levels. This insensitivity of squish volume UHC to load implies that UHC emissions from over-lean regions (apart from the crevice) are not significant for the baseline operating load and above. Likewise, lack of an increase in UHC at the highest load indicates that over-rich regions are generally not problematic at this condition. Despite the low levels of squish volume UHC signal observed at the higher loads, when weighted by cylinder volume it continues to be likely that squish volume UHC remains the dominant source of engine-out UHC emissions.

The continuous decrease in squish volume CO signal with increasing load indicates that the squish region is generally lean overall at the baseline load and below. Unlike the UHC emissions, over-lean regions do appear to impact squish volume CO at the lower loads, since CO is significantly reduced at the highest load. Although heat losses in the squish volume make a quantitative comparison uncertain, correlating the different behavior seen in the UHC and CO emissions to the results of Fig. 4 indicates that the equivalence ratio within the squish volume is likely in the range of 0.3–0.4 at the baseline operating condition. While there is no direct

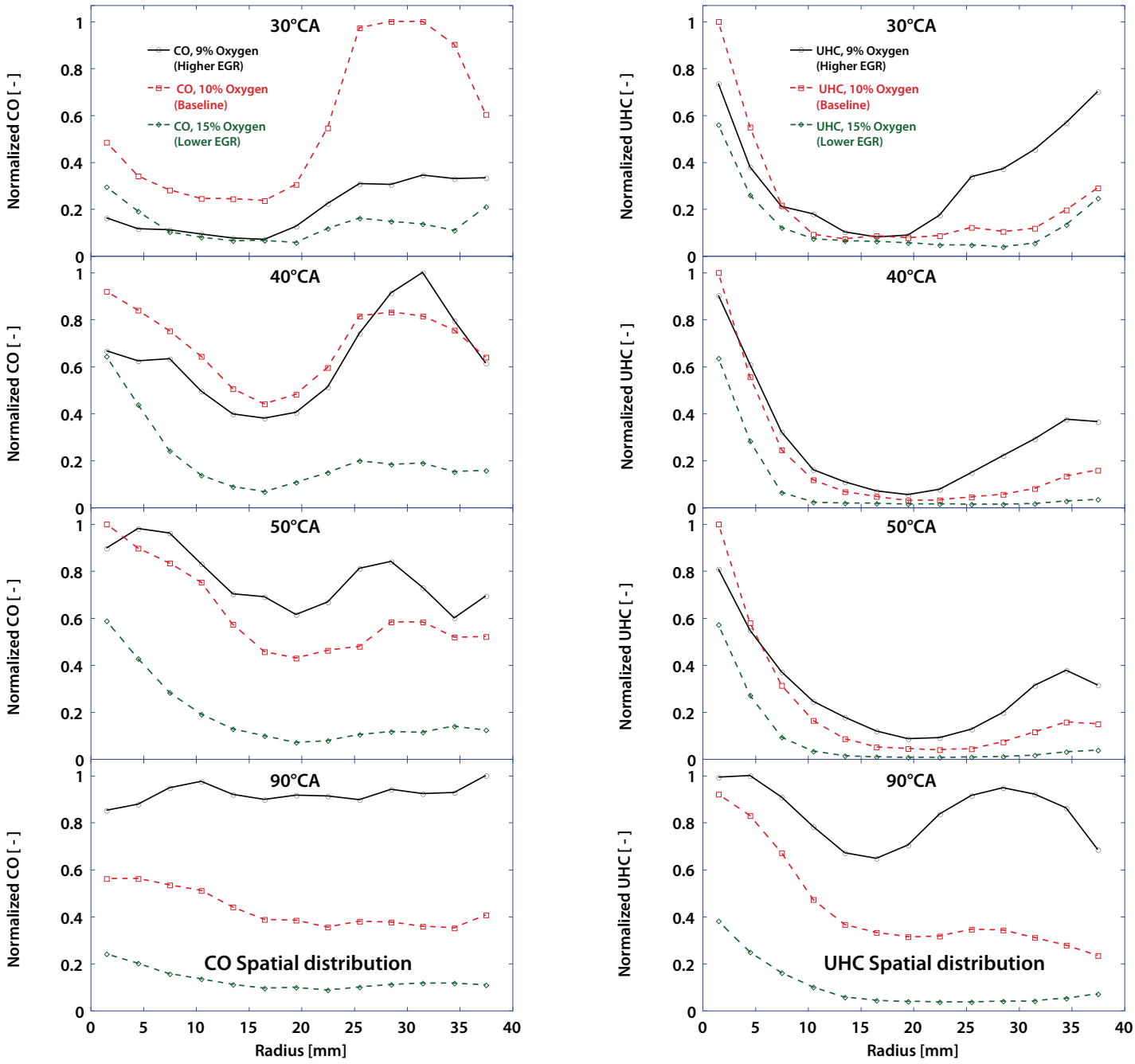

Figure 16 CO and UHC signal levels measured at various levels of charge dilution, but with fixed load and injection timing

evidence that rich mixtures are not formed in the squish volume at the highest load, we deem this unlikely and the results of Fig. 4 suggest that, due to the clear observation of CO, the squish volume equivalence ratio does not exceed approximately 0.5.

O_2 concentration sweep

The spatial distributions of CO and UHC fluorescence with various O_2 concentrations, all at the same baseline load and injection timing, are shown in Fig. 16. Centerline UHC signals are consistently lower at the highest (15%) O_2 concentration, thereby demonstrating enhanced UHC oxidation. Enhanced oxidation processes are also suggested by the centerline CO signals, which are generally lower at the higher [O_2]. Better oxidation at higher [O_2] will likely occur when the centerline UHCs are dominated by either over-mixed or under-mixed regions, and cannot be interpreted as evidence supporting one case over another. Little difference is observed near the centerline between the two lower [O_2] cases (9 and 10%) until 90°CA, when it is clear UHC levels in the bulk of the cylinder are considerably higher at the lower [O_2].

Within the squish volume, UHC levels are strongly impacted by just a 1% decrease in [O_2]. Because the load sweep discussed above indicated that the baseline operating condition results in an overall lean mixture within the squish volume, we do not believe that the

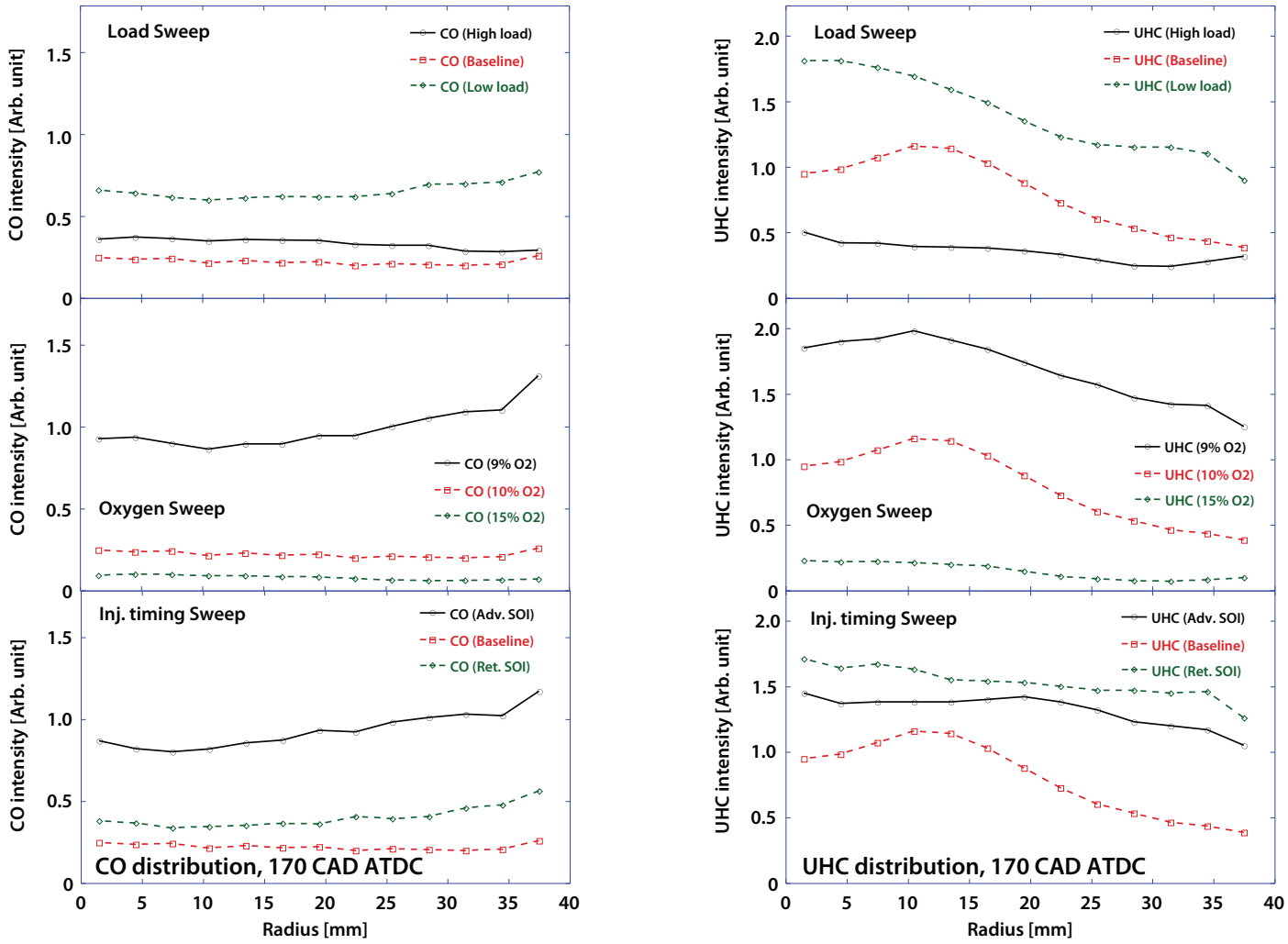

Figure 17 Spatial distributions of CO and UHC measured near the end of cylinder blowdown, 170°CA

increased UHC at the 9% O_2 is caused by mixtures that are now globally rich. Rather, the rate of oxidation of low-to-moderate temperature lean regions slows significantly with dilution—thereby resulting in high UHC levels. The lower CO level observed in the squish region at 30°CA for $[O_2]$=9% is consistent with this interpretation. As the cycle progresses and UHC is oxidized, CO levels increase relative to the baseline case. However, because the rate of conversion of CO to CO_2 is much slower, the CO formed remains largely unoxidized.

At all O_2 concentrations, CO stemming from the squish volume will likely dominate over CO found in the centerline region. At the lower $[O_2]$, UHC emissions are in all probability dominated by the squish volume. However, at 15% $[O_2]$ the squish volume UHC is very low. Moreover, the UHC near the wall, likely emanating from the ring-land crevice, is largely oxidized. In this case, it is possible that UHC emissions are dominated by the centerline region. Thus, for the 15% $[O_2]$, and the still higher oxygen concentrations employed for conventional diesel combustion, the traditional view that leakage from the injector is the more important contributor to total UHC is not inconsistent with the UHC images obtained.

EXHAUST PROCESS LIF MEASUREMENTS

Changes in gas temperature and pressure during the exhaust stroke will likely be sufficiently small that ground state population distributions, quenching processes, and gas density are only changed marginally. By 170°CA, the cylinder pressure has reached its mean value during the exhaust process (1.7 bar) and varies by only ±0.2 bar thereafter due to the influence of wave dynamics. During this period, a qualitative comparison of LIF signal magnitude can be informative. To aid in making this comparison, the CO and UHC LIF signals measured during the exhaust process are presented without normalization.

Radial spatial distributions of CO and UHC fluorescence measured at 170°CA are shown in Fig. 17. At this crank angle, one-dimensional flow modeling (WAVE 7.1) indicates that the initial cylinder blowdown process is nearly complete, but the reverse flow back into the cylinder from the exhaust ports has not yet begun [31]. These distributions are thus representative of the

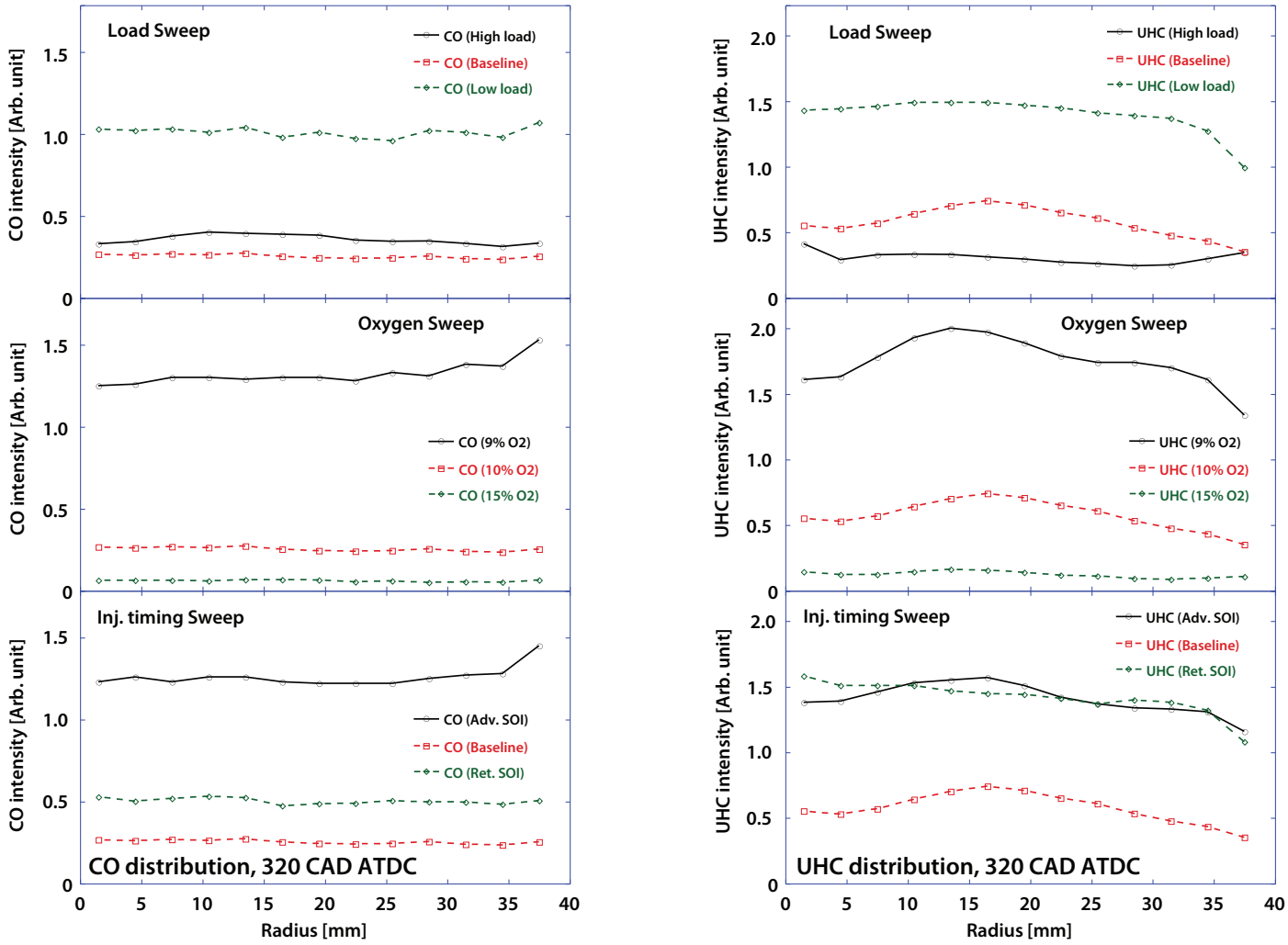

Figure 18 Spatial distributions of CO and UHC measured near the end of the exhaust stroke

contents of the upper-central portion of the cylinder at the start of the exhaust stroke. The uppermost region, comprising approximately 20% of the cylinder mass, was exhausted during the blowdown process.

Generally, both the CO and UHC spatial distributions are approximately uniform, although notable radial gradients can still be seen in the UHC distributions for the baseline case, the light load, and the lower O_2 concentration—highlighting the persistent high UHC concentrations near the cylinder center under these conditions. Due to the presence of these gradients, the signal level must be weighted by the local radial coordinate in order to obtain an appropriate volumetrically-averaged signal level.

The radial distributions of CO and UHC fluorescence measured at 320°CA are shown in Fig. 18. These distributions are representative of the composition of the gases that were in the lower portion of the cylinder at the beginning of the exhaust stroke. The relative magnitude of the signal levels observed as various parameters vary typically follows the same trends observed in Fig. 17. Differences exist in the absolute levels, however, indicating that at the beginning of the exhaust stroke axial gradients in CO and UHC concentrations exist within the cylinder. A characteristic emission level for each operating condition was therefore obtained by computing volumetrically-weighted radial averages of the CO and UHC measured at both 170 and 320°CA, and averaging the results of the two crank angles.

The results obtained are plotted against O_2 concentration in the upper portion of Fig. 19, while the engine-out emissions measured more conventionally [18] are shown in the lower portion. The emission trends are in good general agreement, though the LIF measurements show a larger increase as $[O_2]$ is decreased from 10% to 9% relative to the increase seen from 15% to 10%.

Engine-out emissions were not measured for the same load and SOI sweeps at which the optical measurements were obtained. Nevertheless, as discussed earlier, an optimal injection timing has been identified and closely examined at a similar low temperature operating condition characterized by a higher speed and load [5,17]. Because the physical processes responsible for the existence of an optimal injection timing—overly rich mixtures dominating in the squish volume at early injection and overly lean mixtures

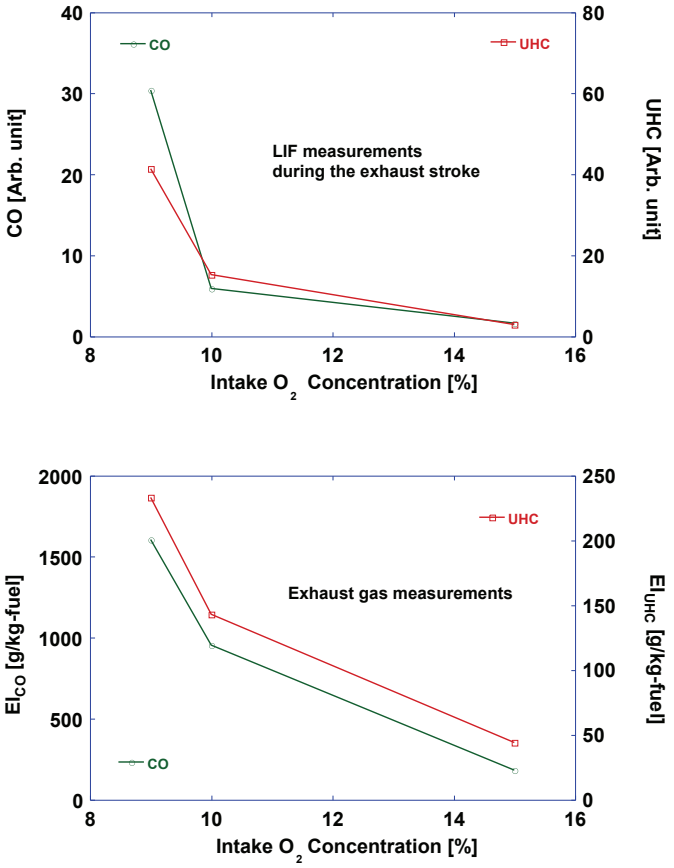

Figure 19 Comparison of the average, volumetrically-weighted CO and UHC emissions measured during the exhaust stroke with engine-out emissions measurements

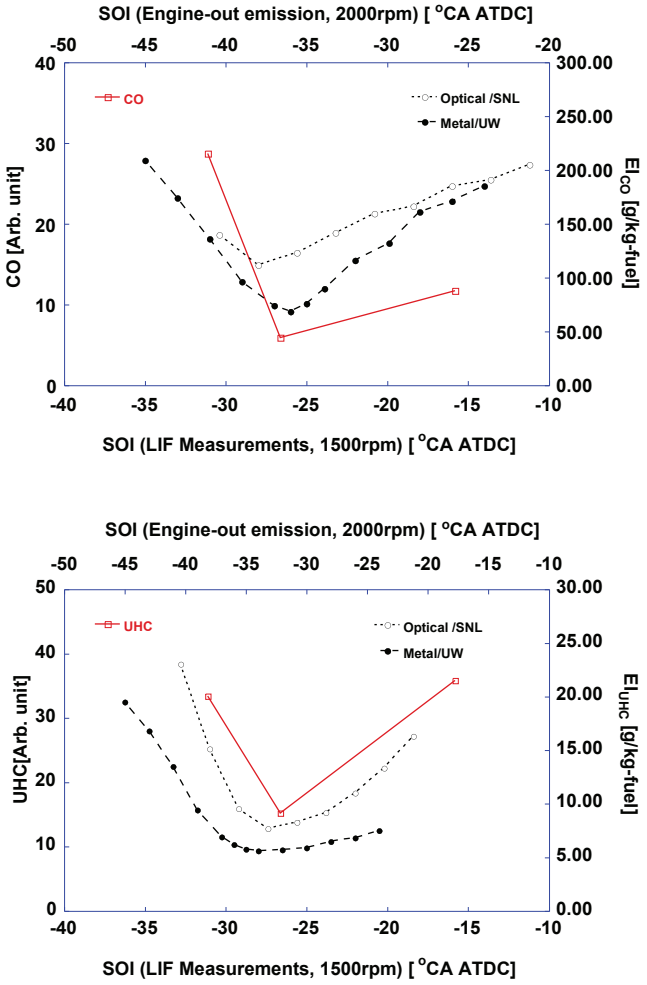

Figure 20 Comparison of the average, volumetrically-weighted CO and UHC emissions measured during the exhaust stroke with engine-out emissions measurements obtained at a similar low-temperature operating condition. Note that separate injection timing axes are employed in order to facilitate the comparison between the two data sets.

dominating with retarded injection—can be expected to be similar for both operating conditions, we can expect similar trends in the engine out emissions.

Figure 20 compares the engine-out CO and UHC emission behavior deduced from the LIF measurements with the engine-out emissions measured for the higher speed and load condition. It is clear that the trends and relative magnitude of the changes in emissions observed correlate well between the LIF measurements and the conventional emissions measurements.

A final, noteworthy aspect the exhaust stroke measurements presented in Figs. 17 and 18 is the magnitude of the axial gradients in CO and UHC indicated by the LIF measurements. Figure 21 presents the variation in the volumetrically-averaged CO and UHC distributions with crank angle, or—equivalently—with axial location in the cylinder. In general, the magnitude of the axial gradients observed is small.

Two of the operating conditions investigated in this study for the O_2 sweep (10% and 15% O_2) have also been examined using a fast FID to measure exhaust gas hydrocarbons in the exhaust port [31], approximately 25 mm from the exhaust valve stem. From these data, information on the spatial locations of UHC in the cylinder can be extracted. In contrast to the results shown in Fig. 21, which show little change or slightly lower UHC low in the cylinder, the FID measurements suggest that exhaust gas UHC concentrations low in the cylinder (late in the exhaust stroke) are about 25% higher. The difference between these studies may be associated with mixing processes in the port. With skip-fired operation, the first exhaust gases entering the port mix with the residual from the previous motored cycles, which is very low in UHC. Consequently, the exhaust gas UHC concentrations measured with the FID early in the exhaust process could be under-estimated.

CONCLUSIONS

Laser-induced fluorescence can be successfully applied in diesel engines operating with realistic fuels to visualize the in-cylinder spatial distributions of CO. The spectral characteristics of the fluorescent emissions show that the CO emissions near 450 nm and 483 nm can be successfully separated from other interfering species, with the exception of a broadband background due to PAH fluorescence. This background can be

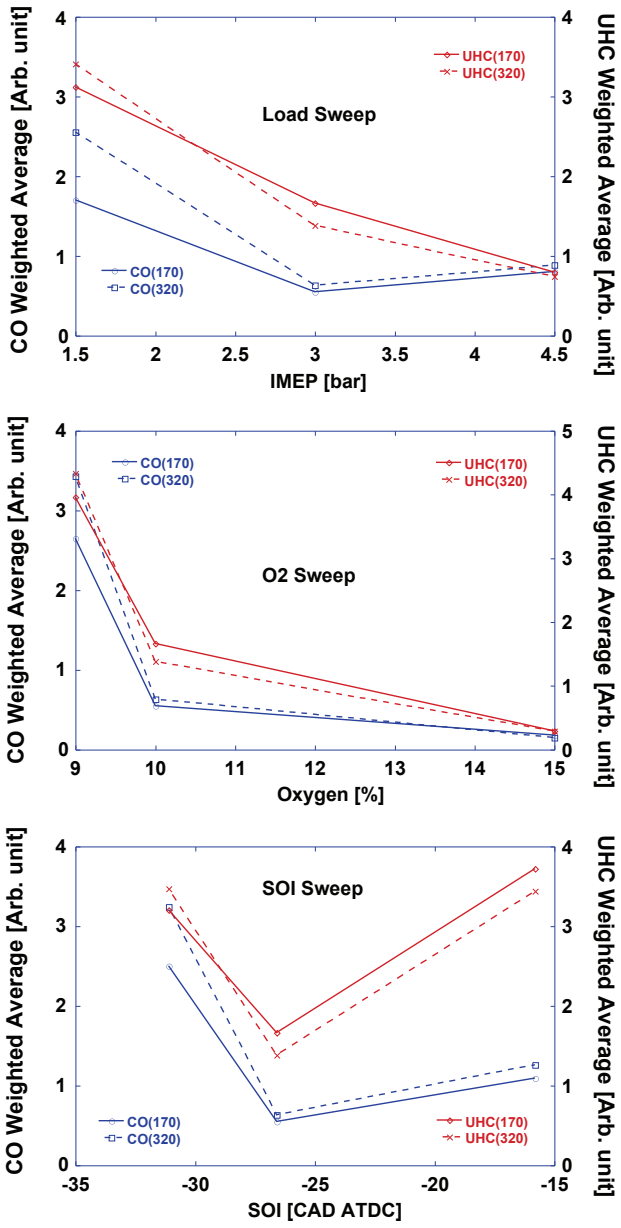

Figure 21 Comparison of the average, volumetrically-weighted CO and UHC emissions measured during the exhaust stroke at two crank angles, 170 and 320°CA. The difference is representative of the axial stratification of each species within the cylinder.

eliminated by either appropriate spectral filtering in combination with subtraction of an off-line image, or by acquisition of spectrally-resolved data. The necessity of correcting for the background interference impedes single-cycle CO imaging, though signal levels are generally adequate. In addition to broadband PAH fluorescence, the interfering emissions contain contributions from C_2 and CH emissions—all of which represent a measure of UHC.

A complex dependency of the CO fluorescence signal on pressure, temperature, and composition prevents a fully-quantitative interpretation of the data, and quantification of the UHC fluorescence comprising the background emissions is still more difficult. Nevertheless, the measurements clarify the regions within the cylinder where high CO and UHC concentrations are found, and, in many cases, a judgment as to the relative importance of these regions to engine-out emissions can be made. Furthermore, by examining the spatial and temporal evolution of the UHC and CO fluorescence as various parameters are varied, a reasoned determination of the local mixture state (rich or lean) can be achieved.

For the PPCI operating condition investigated, the following behavior is observed during the expansion stroke:

- The spatial distribution of UHC within the clearance volume is dominated by a region near the cylinder centerline and by a region near the cylinder wall, the latter likely due to UHC released from the top ring-land crevice. When injection timing is advanced or retarded from MBT timing, UHC extends throughout the squish volume, due to formation of over-rich or over-lean mixtures, respectively. The behavior of the UHC distributions as load is varied indicates that, at light load, the centerline UHC has a significant contribution stemming from lean mixture. Within the squish volume, increasing load has little impact on UHC until late in the expansion stroke, while higher UHC is observed at lower load. Increased dilution slows oxidation throughout the cylinder, but most noticeably within the squish volume—significantly increasing UHC emissions from this region.

  Despite quantitative uncertainty, the data suggest that UHC emissions stemming from the squish volume and ring-land crevice dominate over the centerline region. The exception occurs at higher O_2 concentration, when squish volume UHC is low and enhanced crevice volume UHC oxidation is observed.

- CO is generally observed near the cylinder centerline and broadly distributed within the squish volume. Advanced injection timing increases squish volume CO; retarded injection does likewise, although not until later in the cycle. The variation in CO with load demonstrates that the squish volume mixture is lean at the baseline load and below. Moreover, a comparison of the joint behavior of the UHC and CO signals with load to homogeneous reactor simulation results indicates that at the baseline load the squish volume mixture has an equivalence ratio between roughly 0.3 and 0.4. As seen in the UHC behavior, increased dilution generally increases CO throughout the cylinder, but especially within the squish region.

  The data indicate that at all operating conditions investigated, CO emissions stemming from the squish region outweigh those stemming from the cylinder centerline region.

The volumetrically-averaged LIF signals of both CO and UHC obtained within the exhaust stroke correlate well with available exhaust gas measurements. Insignificant

differences in the CO and UHC concentrations between the upper and lower portions of the cylinder are observed at the start of the exhaust stroke.

ACKNOWLEDGMENTS

Support for this research was provided by the United States Department of Energy (Office of Vehicle Technologies), by a Korea Research Foundation Grant funded by the Korean Government (MOEHRD KRF-2006-352-D00036), and by General Motors Corporation (agreement FI083070326). This study was performed at the Combustion Research Facility, Sandia National Laboratories in Livermore, California. Sandia is a multiprogram laboratory operated by Sandia Corporation, a Lockheed Martin Company, for the United States Department of Energy's National Nuclear Security Administration under contract DE-AC04-94AL85000. The authors thank Seungmook Oh from the Korea Institute of Machinery and Materials for his assistance with the initial development of the CO LIF diagnostic, Mark Musculus of Sandia National Laboratories for helpful discussions regarding sources of UHC emissions, and the many members of the GM-UW Cooperative Research Laboratory program for their insight and comments. Kenneth St.Hilaire, Dave Cicone, Chris Carlen and Gary Hubbard of Sandia National Laboratories also provided invaluable technical assistance in the laboratory.

REFERENCES

1. Akihama, K., Takatori, Y. and Inagaki, K., "Mechanism of the Smokeless Rich Diesel Combustion by Reducing Temperature," SAE paper 2001-01-0655, 2001.
2. Noehre, C., Andersson, M., Johansson, B. and Hultqvist, A., "Characterization of Partially Premixed Combustion," SAE paper 2006-01-3412, 2006.
3. Kook, S., Bae, C., Miles, P. C., Choi, D. and Pickett L. M., "The Influence on Charge Dilution and Injection Timing on Low-Temperature Diesel Combustion and Emissions," SAE paper 2005-01-3837, 2005.
4. Kook, S., Bae, C., Miles, P. C., Choi, D., Bergin, M. and Reitz, R., "The Effect of Swirl Ratio and Fuel Injection Parameters on CO Emission and Fuel Conversion Efficiency for High-Dilution, Low-Temperature Combustion in an Automotive Diesel Engine," SAE paper 2006-01-0197, 2006.
5. Opat, R., Ra, Y., Gonzalez D., M. A., Krieger, R., Reitz, R. D. and Foster, D. E., "Investigation of Mixing and Temperature Effects on HC/CO Emissions for Highly Dilute Low Temperature Combustion in a Light Duty Diesel Engine," SAE paper 2007-01-0193, 2007.
6. Kitamura, T., Ito, T., Senda, J., and Fujimoto, H., "Mechanism of Smokeless Diesel Combustion with Oxygenated Fuels Based on the Dependency of the Equivalence Ratio and Temperature on Soot Particle Formation", *International Journal of Engine Research*, Vol. 3, No. 4, pp.223-247, 2002.
7. http://www-cmls.llnl.gov/?url=science_and_technolog y-chemistry-combustion-nc7h16
8. Park, S.W. and Reitz, R.D., "Numerical Study on the Low Emission Window of Homogeneous Charge Compression Ignition Diesel Combustion," *Combustion Science and Technology*, vol.179, no.11, pp.2279-2307, 2007.
9. Golovitchev, V.I., Montorsi, L., Calik, A.T. and Milani, M., "The EGR Effects on Combustion Regimes in Compression Ignited Engines," SAE paper 2007-24-0040, 2007.
10. Sjöberg, M. and Dec, J.E., "An Investigation into Lowest Acceptable Combustion Temperatures for Hydrocarbon Fuels in HCCI Engines," *Proc. of the Combustion Institute*, vol. 30, pp.2719-2726, 2005.
11. Khan, I.M., Greeves, G. and Wang, C.H.T., "Factors Affecting Smoke and Gaseous Emissions from Direct Injection Engines and a Method of Calculation," SAE paper 730169, 1973.
12. Greeves, G., Khan, I.M., Wang, C.H.T. and Fenne, I., "Origins of Hydrocarbon Emissions from Diesel Engines," SAE paper 770259, 1977.
13. Musculus, M.P.B., Lachaux, T., Pickett, L.M. and Idicheria, C.A., "End-of-Injection Over-Mixing and Unburned Hydrocarbon Emissions in Low-Temperature-Combustion Diesel Engines," SAE paper 2007-01-0907.
14. Tsurushima, T., Zhang, L., and Ishii, Y., "A Study of Unburnt Hydrocarbon Emission in Small DI Diesel Engines," SAE paper 1999-01-0512, 1999.
15. Montajir, R.M., Tsunemoto, H., Ishitani, H., Koji, T., and Kenichi, K., "A New Combustion Chamber Concept for Low Emissions in Small DI Diesel Engines," SAE paper 2001-01-3263, 2001.
16. Kashdan, J.T., Mendez, S., and Bruneaux, G., "On the Origin of Unburned Hydrocarbon Emissions in a Wall Guided, Low NO_x Diesel Combustion System," SAE paper 2007-01-1836, 2007.
17. Colban, W.F., Kim, D., Miles, P.C., Oh, S., Opat, R., Krieger, R., Foster, D., Durrett, R.P., and Gonzalez, M.A., "A Detailed Comparison of Emissions and Combustion Performance between Optical and Metal Single-Cylinder Diesel Engines at Low-Temperature Combustion Conditions," SAE paper 2008-01-1066, 2008.
18. Colban, W. F., Miles, P. C., and Oh, S., "Effect of Intake Pressure on Emissions from an Automotive Diesel Engine Operating in Low Temperature Combustion Regimes," SAE paper 2007-01-4063, 2007.
19. Aldén, M., Wallin, S., and Wendt, W., "Applications of Two-Photon Absorption for Detection of CO in

Combustion Gases," *Appl. Phys. B*, Vol. 33, pp.205-208, 1984.

20. Seitzman, J.M., Haumann, J., and Hanson, R.K., "Quantitative Two-Photon LIF Imaging of Carbon Monoxide in Combustion Gases," *Applied Optics*, Vol. 26, pp. 2892-2899, 1987.
21. Rehm, J.E. and Paul, P.H., "Reaction Rate Imaging," *Proc. of the Combustion Institute*, Vol. 28, pp.1775-1782, 2000.
22. Everest, D.A., Shaddix, C.R., and Smythe, K.C., "Quantitative Two-Photon Laser-Induced Fluorescence Imaging of CO in a Flickering CH4/Air Diffusion Flame," *Proc. of the Combustion Institute*, Vol. 26, pp.1161-1169, 1996.
23. Richter, M., Li, Z.S., Aldén, M., "Application of Two-Photon Laser-Induced Fluorescence for Single-Shot Visualization of Carbon Monoxide in a Spark Ignited Engine," *Applied Spectroscopy*, Vol. 61, pp.1-5, 2007.
24. Settersten, T.B., Dreizler, A., and Farrow, R.L., "Temperature- and Species-Dependent Quenching of CO *B* Probed by Two-Photon Laser-Induced Fluorescence using a Picosecond Laser," *J. Clem. Phys*., Vol. 117, No. 7, pp.3173-3179, 2002.
25. Nefedov, A.P., Sinel'shchikov, V.A., Usachev, A.D., and Zobnin, A.V., "Photochemical Effect in Two-Photon Laser-Induced Fluorescent Detection of Carbon Monoxide in Hydrocarbon Flames," *Appl. Optics*, Vol. 37, pp.7729-7736, 1998.
26. Petarca, L. and Marconi, F., "Fluorescence Spectra and Polycyclic Aromatic Species in a n-Heptane Diffusion Flame," *Combustion and Flame*, Vol. 78, pp.308-325, 1989.
27. Lachaux, T. and Musculus, M.P.B., "In-Cylinder Unburned Hydrocarbon Visualization during Low-Temperature Compression-Ignition Engine Combustion using Formaldehyde PLIF," *Proc. Combust. Inst.,* Vol. 31, pp.2921-2929, 2007.
28. Miles, P.C., Collin, R., Hildingsson, L., Hultqvist, A., and Andersson, Ö., "Combined Measurements of Flow Structure, Partially Oxidized Fuel, and Soot in a High-Speed, Direct-Injection Diesel Engine," *Proc. Combust. Inst.,* Vol. 31, pp.2963-2970, 2007.
29. Hildingsson, L., Hultqvist, A., and Miles, P., "The Effect of Swirl and Injection Phasing on Flow Structures and Mixing in an HSDI Diesel Engine," Proc. of Thermo- and Fluid-dynamic Processes in Diesel Engines, THIESEL 2006, Valencia, Sept. 12-15, 2006.
30. Bergin, M.J. and Reitz, R.D. Private communication, 2005.
31. Colban, W.F., Miles, P.C., and Oh, S., "On the Cyclic variability and Sources of Unburned Hydrocarbon Emissions in Low Temperature Diesel Combustion Systems," SAE paper 2007-01-1837, 2007.